FUNCTIONAL PHOTOACOUSTIC MICROSCOPY

A Dissertation

by

HAO ZHANG

Submitted to the Office of Graduate Studies of
Texas A&M University
in partial fulfillment of the requirements for the degree of

DOCTOR OF PHILOSOPHY

August 2006

Major Subject: Biomedical Engineering

FUNCTIONAL PHOTOACOUSTIC MICROSCOPY

A Dissertation

by

HAO ZHANG

Submitted to the Office of Graduate Studies of
Texas A&M University
in partial fulfillment of the requirements for the degree of

DOCTOR OF PHILOSOPHY

Approved by:

Chair of Committee,	Lihong Wang
Committee Members,	Hsin-i Wu
	James Moore Jr.
	Steven Wright
Head of Department,	Gerard L. Coté

August 2006

Major Subject: Biomedical Engineering

ABSTRACT

Functional Photoacoustic Microscopy. (August 2006)

Hao Zhang, B.Eng., Shanghai JiaoTong University;

M.Eng., Shanghai JiaoTong University

Chair of Advisory Committee: Dr. Lihong Wang

This dissertation focuses on laser-based noninvasive photoacoustic microscopy of subsurface structures *in vivo*. Photoacoustic microscopy is a hybrid imaging modality that combines the high-resolution advantage of ultrasonic imaging in deep tissue with the high-contrast advantage of optical imaging. It detects the short-pulsed laser-induced photoacoustic waves, whose amplitudes reflect the localized laser energy absorption, to image the internal optical absorption distributions. The spatial resolution is determined by the ultrasonic focal ability and the ultrasonic bandwidth. The imaging depth is primarily limited by the acoustic attenuation within the reach of diffuse photons. The ratio of maximum imaging depth to axial resolution in photoacoustic microscopy is greater than 100, which is comparable to that of modern high-resolution optical imaging modalities, such as confocal microscopy, two-photon microscopy, and optical coherence tomography. However, the maximum imaging depth has been much enlarged by taking advantages of absorbed diffuse photons. Based on the intrinsic optical contrast, we have achieved *in vivo* volumetric imaging of subcutaneous microvasculature, skin melanoma, and acute thermal injuries in high spatial resolution. We have imaged physiological parameters in subcutaneous microvessels, such as total hemoglobin concentration and hemoglobin oxygen saturation, on a single vessel basis in small animals *in vivo*. We have also monitored changes of hemoglobin oxygen concentration between different systemic physiological states on a vessel-by-vessel basis. Moreover, we have demonstrated the feasibility of human imaging using photoacoustic microscopy by imaging finger tips and subcutaneous palm vessels.

DEDICATION

This work is dedicated to my parents and my wife
who have made it possible.

ACKNOWLEDGEMENTS

I wish to express my sincere gratitude to my advisor, Dr. Lihong Wang, for his support, guidance, encouragement, and countless time he has spent for me through all my years as a graduate student. It goes without saying that his knowledge and experience have been indispensable.

I am also grateful for Dr. Konstantin Maslov, who has been a mentor, a colleague, and a friend. Without his ingenious design and generous instruction, this dissertation would not be possible. I would like to thank Dr. Hsin-i Wu, Dr. James Moore Jr., and Dr. Steve Wright, who have sacrificed time and energy to serve on my committee, and Dr. George Stoica, who has supported all my animal experiments. I would also like to thank Dr. Geng Ku, Mrs. Gina Lungu, Dr. Ovidiu Cracuin, Dr. Jung-taek Oh, Dr. Meng-Lin Li, and all members in the Optical Imaging Laboratory for their assistance and contribution to my dissertation. This work is sponsored by National Institutes of Health grants R01 EB000712 and R01 NS46214.

TABLE OF CONTENTS

Page

CHAPTER Page

LIST OF TABLES

LIST OF FIGURES

CHAPTER I

INTRODUCTION

1. Motivation

Optical imaging presents several potential advantages over existing radiological techniques. First, optical irradiation is nonionizing. Hence, reasonable dosage can be applied to patients repeatedly without harmful side effects. Second, based on optical scattering or absorption contrast, different types of soft tissues can be distinguished by optical imaging whereas other modalities cannot. Moreover, optical contrast is usually highly correlated with physiological changes in biological tissues, which gives optical techniques high sensitivity in functional imaging. As a result, optical imaging has the potential in detecting abnormality and physiological changes in tissues, for example cancer in early stages.[1]

Optical properties include optical scattering and optical absorption. Optical scattering is strongly related to the cellular or sub-cellular structures of tissue such as size and density of cell nucleus.[2-4] Optical absorption depends on the absorbing biochemical compounds presented in biological tissue. Within the visible and near-infrared regions, the dominating intrinsic absorbing pigments in tissue are hemoglobin and melanin. For example, the optical absorption contrast between the blood and the surrounding soft tissues can be as high as 1000% for the 850-nm wavelength light.[5] The optical absorption contrast between tumors and surrounding normal tissues can be as

---

This dissertation follows the style and format of Applied Optics.

high as 300% for NIR light[6] and even higher in the visible region due to the high blood content in malignant tumors. Therefore, imaging techniques based on optical-absorption contrast can be used to reveal hemoglobin-related metabolic processes, such as changes of total hemoglobin concentration and hemoglobin oxygen saturation (SO_2),[7,8] to image tumor angiogenesis. It can also be applied to detect melanin-related skin melanoma cancers. Furthermore, by employing exogenous bioactive optical contrast agents, optical imaging has the potential to detect subtle functional changes in living tissue at the molecular or genetic level.

However, due to the strong scattering of light in biological tissue, how to achieve high spatial resolution and a large imaging depth still remains a challenging problem. Existing high resolution optical imaging modalities include confocal microscopy,[9-11] two-photon microscopy,[12,13] and optical coherence tomography (OCT).[14] Confocal microscopy and two-photon microscopy rely on ballistic photons (photons that travel along an undeviated path in a medium without being scattered) to provide high spatial resolution. Using coherence gating, OCT can image deeper by detecting singly backscattered photons. However, most of the biological tissues, excluding ocular tissue, have scattering coefficients ranging from 10 cm^{-1} to 100 cm^{-1} depending on the optical wavelength used.[15] After propagating about one optical transport mean free path (~1 mm in soft biological tissues at visible and near-infrared wavelengths) in biological tissues, photons are multiply scattered and, hence, randomly distributed. Therefore, imaging depths of existing high-resolution optical imaging modalities in scattering biological tissue are fundamentally limited to approximately 1 mm. Beyond this depth limit, none of these imaging techniques are capable of achieving high depth resolution. Tremendous efforts have been undertaken to overcome this fundamental limit of imaging depth, but results are still unsatisfactory. Although diffuse optical tomography (DOT) can detect the diffuse photons to achieve larger imaging depth up to several centimeters,[16] its poor depth-dependent spatial resolution makes it unsuitable for structural imaging. Therefore, finding a new technique to overcome this long-standing fundamental depth limitation was the impetus for this dissertation.

Since it is impractical to localize diffuse photons at high spatial resolution directly, an indirect detection method may solve this problem. Compared with optical scattering, ultrasonic scattering is 2-3 orders of magnitude weaker in biological tissues. Therefore, high-frequency ultrasonic imaging provides better spatial resolution in deep biological tissues than existing optical imaging. As a result, imaging modalities combining optical contrast with ultrasonic detection provide good alternatives to realize high-resolution imaging of optical properties at large depth in biological tissues. Photoacoustic imaging (PAI)[1,5,6, 17 - 25] and ultrasound modulated optical tomography (UOT)[26-28] are two examples of such hybrid techniques that have been explored in the past decades. They both rely on ultrasonic localization to provide a much improved spatial resolution in the diffuse regime than pure optical technologies do, while PAI images the optical absorption contrast and UOT images the optical scattering contrast. In other words, these techniques combine the optical contrast with the ultrasonic resolution in deep biological tissue.

2. Photoacoustic imaging

PAI is a noninvasive imaging technique that detects absorbed diffuse photons ultrasonically through a photoacoustic (PA) effect.[29] Although PA wave can be generated by both amplitude-modulated continuous-wave (CW) laser and short-pulsed laser,[30] most of the existing PAI use short-pulsed laser as the radiation source and detect the induced time-resolved PA signal for imaging purposes. The duration of the laser pulse is shorter than the time needed for acoustic wave to propagate the distance that equals to the desirable spatial resolution. A typical value of laser pulse duration in PAI is several nanoseconds.

When a short-pulsed laser irradiates biological tissue, wideband PA waves are generated as a result of transient thermoelastic expansion inside the tissue. Therefore the ultrasonic detector employed must have a comparable large bandwidth and approximately equal detection sensitivity over the entire frequency band to achieve high spatial resolution. The axial resolution (along the direction of ultrasound propagation) of PAI is determined by the bandwidth of the ultrasonic detector. When a non-focused ultrasonic detector or a detector array is used, the lateral resolution (along the direction perpendicular to the direction of ultrasound propagation) is determined by the dimension of the ultrasonic detector, or the dimension and geometry of the ultrasonic transducer array. If a focused ultrasonic detector is used, the lateral resolution is defined by the detector’s focal ability. The magnitude of the detected PA waves is proportional to the localized optical energy absorption in the tissue, which can be, subsequently, used to visualize or quantitatively characterize various tissue structures and their physiological functions based on optical absorption.

3. History of PAI development

Since the initial theoretical and experimental studies of photoacoustics in the 1970s and the early 1980s,[31] PAI has been widely used in various biomedical applications. Nowadays, the major focus of PAI is on the photoacoustic tomography (PAT),[1,5,6,18,20-23] in which a non-focused ultrasonic detector is used to collect the time-resolved short-pulsed laser induced PA pulses and a inverse reconstruction algorithm is employed to calculate the final two-dimensional (2D) or three-dimensional (3D) images. Various experiments in biological tissue using PAT have been conducted and significant results have been achieved.

Esenaliev *et al.*[18,32] and Andreev *et al*.[33] have studied small tumors embedded deeply in biological tissue. Beenen *et al*.[34], Oraevsky *et al*.,[35] and Karabutov *et al*.[36] have imaged layered tissues in an attempt to advance towards *in vivo* detection of skin cancer. Hoelen *et al*. have applied photoacoustic technique to image blood vessels in 3D with a 1-cm imaging depth and a good axial resolution. Paltauf *et al.*[37] adopted an optical method instead of piezoelectric devices for two-dimensional ultrasonic detection. In 2003, Kolkman *et al*.[38] have achieved, for the first time, *in vivo* photoacoustic imaging of blood vessels in humans. Functional measurement of SO_2 using PA method on both *in vitro* and *in vivo* blood has been achieved by Fainchtein *et al*.,[39] Esenaliev *et al*.,[40,41] and

Petrov *et al*.,[42] based on single wavelength measurement, and by Wang *et al.*[43] based on multi-wavelength spectroscopic measurement.

In 2005, a new geometry different from all aforementioned PAI, referred to as photoacoustic microscopy (PAM), was developed by Maslov *et al*. High spatial-resolution images of subcutaneous blood vessels in rats were acquired *in vivo* with a lateral resolution of 45 µm, an axial resolution of 15 µm, and a maximum imaging depth of 3 mm. Compared with the previous PAI, PAM works in reflection (backward) mode rather than orthogonal or transmission mode, employs high-frequency focused ultrasonic detector, provides real-time A-lines, and requires no image reconstruction. Compared with the previous confocal microscopic PA imaging technologies,[44] PAM has achieved much improved image quality at a greater depth. This dissertation will focus on applying PAM to various biological tissues to achieve both structural and functional imaging *in vivo* in animals and to demonstrate the feasibility of human imaging.

CHAPTER II

PAM SYSTEM

1. Introduction

PAM is a reflection mode PA technology that employs a high-frequency focused ultrasonic transducer and dark-field illumination to detect short-pulsed laser-induced PA waves for both structural and functional imaging. Although high image resolution was achieved previously with a full 360 degree circular-scanning PAT around an object with minimal artifacts, it can be accomplished only with elevated objects, such as brain or breast. Some planner scanning mode PA imaging [38,44] have also been investigated before, which are not limited by the shape of the sample. However, their image qualities are not very impressive. The major reason for such degraded image quality comes from the strong optical absorption on skin surface, which leads to ultrasonic reverberation and potential overshadowing of the much weaker PA signals generated from deep structures.

In PAM, the dark-field light illumination and ultrasonic detection are placed at the same side with a confocal geometry. The induced PA sources are localized with high spatial resolution by a strongly spherically focused ultrasonic transducer. By recording the time-resolved PA signal and raster scanning the ultrasonic transducer, a three-dimensional (3D) image is acquired. Similar to traditional acoustic microscopy,[45] the lateral resolution of PAM is determined by the ultrasonic focal diameter, and the axial resolution is inversely related to the bandwidth of the ultrasonic transducer. Therefore, PAM requires a wideband, high-frequency ultrasonic transducer to achieve high spatial resolutions. Because of the strong frequency-dependent acoustic attenuation at central frequencies higher than 10 MHz, the maximum imaging depth of PAM will be limited by the ultrasonic penetration depth, rather than the optical penetration depth of the diffuse photons. Hence, both the spatial resolutions and the maximum imaging depth of PAM will be scaleable with the ultrasonic parameters within the reach of diffuse photons.

2. Experimental setup and scanning method

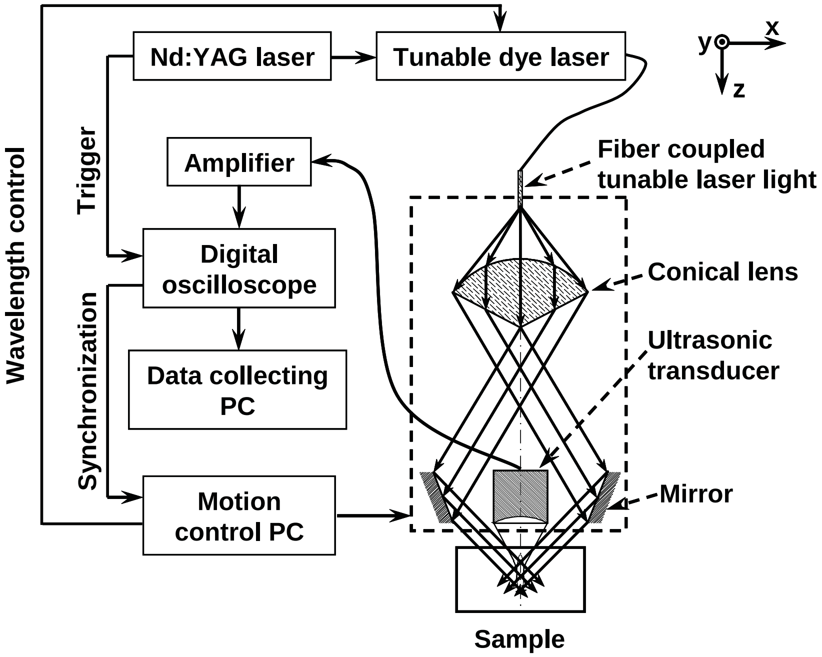

Fig. 1. Schematic of the PAM system.

The schematic of the experimental setup is shown in Fig. 1. PAM uses a tunable dye laser (ND6000, Continuum, CA), pumped by an Nd:YAG laser (Brilliant B, Bigsky, MT; pulse duration: 6.5 ns; repetition rate: 10 Hz) as the radiation source. Laser light at designated wavelengths (wavelength range: 570-800 nm) was transmitted through an optical fiber and expanded by a conical lens to form an annular beam, which was then weakly focused into the tissue.

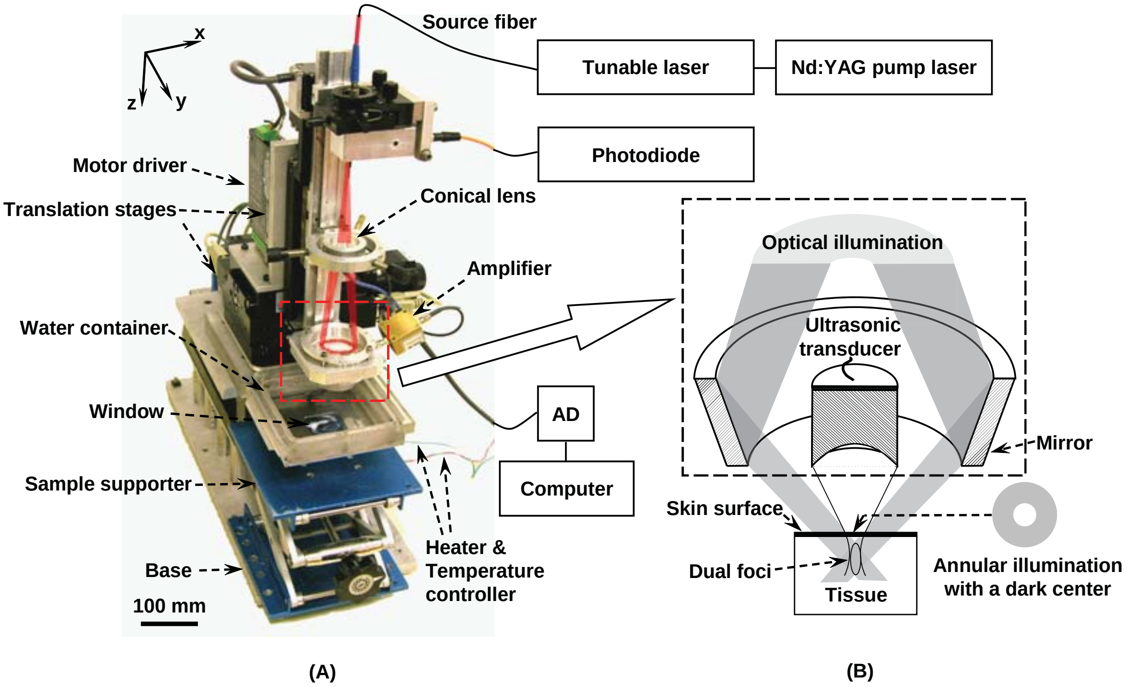

Fig. 2. Experimental PAM system. (A) Photograph of the imaging system. (B) Formation of the dark-center optical illumination on tissue surface and the optical-ultrasonic dual foci inside tissue.

The optical illumination was donut-shaped so that no strong PA signals were produced from the illumination center on the skin surface. A spherically focused ultrasonic transducer (V214-BB-RM, Panametrics, WA; central frequency: 50 MHz; NA: 0.44; bandwidth: 80% at –6 dB; focal length: 6.7 mm; focal zone: 0.3 mm) was placed coaxially with the laser beam with its focus overlapping the optical focal region. A photograph of the PAM scanning system and a detailed illustration of the formation of the dark-center optical illumination on tissue surface and the optical-ultrasonic dual foci inside tissue are given in Fig. 2. In an optically clear medium, the optical focus was measured to be 2 mm in diameter, which was much wider than the ultrasonic focus. All of the components in the dashed-box in Fig. 1 were raster-scanned in the horizontal (*x*-*y*) plane. The mechanical scanning was controlled by a PC that also directed the tunable dye laser to change wavelengths during data acquisition if necessary. The PA signals received by the ultrasonic transducer were digitized by a digital oscilloscope (TDS 5034B, Tektronix, OR; sampling rate: 250 MHz) after a 24-dB amplification (ZFL-500LN, Mini-Circuits, NY). The pulse energy was controlled to be less than 0.2 mJ and the incident energy density on the sample surface as well as around the optical focus was less than 6 mJ/cm^2, which is well within the ANSI standard.[46]

In *in vivo* experiments, the components within the dashed-box in Fig. 2(A) were translated in a water bath. A window at the bottom of the water container was sealed with an optically and ultrasonically transparent disposable polyethylene membrane (thickness: 0.044 mm). After commercial ultrasound gel (Clear Image Ultrasound Scanning Gel, Sonotech, WA) was applied to the region of interest on the sample for acoustic coupling, the sample was placed between the water container and the sample supporter for imaging.

To acquire an image, the amplitude of the PA wave was recorded for 2 μs at each transducer location and was, subsequently, converted into a depth resolved signal (A-line) along the *z* axis according to the sound velocity in soft tissue (1.54 mm/µs). Therefore, the raster scan in the *x*-*y* plane produced a 3D image. The amplitude of each PA wave was normalized by the energy of the corresponding incident laser pulse.

3. System performances

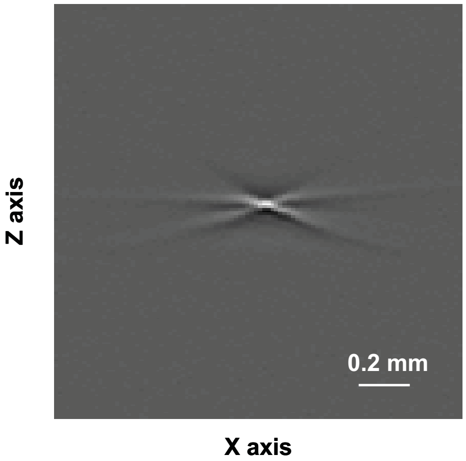

Fig. 3. Cross-sectional image of a 6-µm carbon fiber in an optically scattering solution.

In this confocal geometry as stated previously, the axial resolution of PAM is inversely related to the bandwidth of the ultrasonic transducer. The lateral resolution of PAM is determined by the focal diameter of the ultrasonic transducer since the ultrasonic focus is much smaller than the optical focus. Therefore, in principle, the best lateral resolution that we can achieve is the diffraction-limited ultrasonic resolution. In the traditional acoustic microscopy, the Rayleigh criterion states that the lateral spatial resolution is $0.61(\lambda_0 / NA)$, where λ_0 is the central acoustic wavelength and NA is the numerical aperture. For the 50-MHz transducer we are currently using, the calculated ultrasonic lateral resolution is 35 µm.

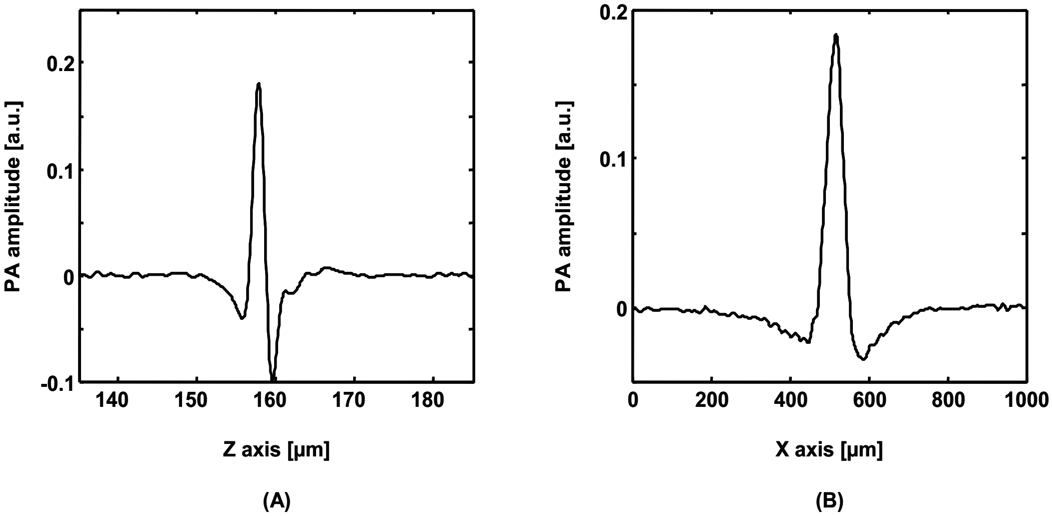

Fig. 4. 1D PSF along the axial (A) and lateral (B) directions.

To quantify the spatial resolution experimentally, we imaged the cross section of a carbon fiber with a diameter of 6 µm in optically scattering solution in two dimensions, which can be treated as a 2D point-spread-function (PSF) of PAM. Then 1D PSFs along both the lateral and axial directions are extracted, and Raleigh criterion is employed to quantify the lateral and axial resolution based on an artificial shift.

Figure 3 shows the B-scan image of the carbon fiber and Fig. 4 shows the 1D PSFs along the axial and lateral directions. Based on a 1D shifting-summation, the axial resolution was calculated to be 15 µm and the lateral resolution was 45 µm. Compared with the theoretical estimation, the calculated lateral resolution was 25% larger, which was resulted from the lack of enough high frequency components in imaging of the carbon fiber. A spectrum of the A-line shown in Fig. 4(A) is shown in Fig. 5, where the central frequency was below 50 MHz.

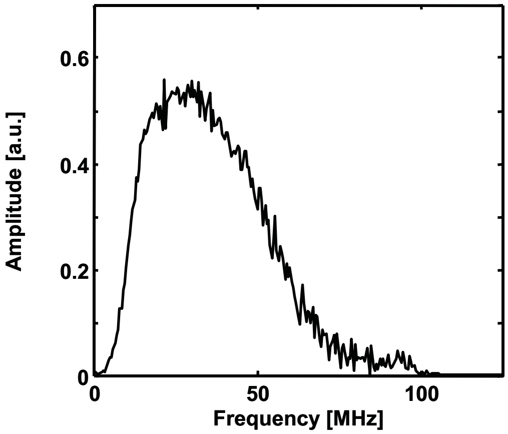

Fig. 5. Spectrum of an A-line acquired from carbon fiber.

The maximum imaging depth of PAM is primarily limited by the ultrasonic attenuation within the reach of diffuse photons. At central frequencies higher than 10 MHz, the acoustic attenuation is frequency-dependent and is stronger than the optical attenuation. A typical value of acoustic attenuation in porcine skin is 2.5 dB/cm MHz,[47] which gives a 12.5 dB/mm attenuation at a central frequency of 50 MHz. To estimate the maximum imaging depth of PAM experimentally, a horse hair with a diameter of 300 μm was embedded into a chicken breast tissue wedge and a series of B-scan images of the horse hair were acquired. Then signal-to-noise ratio (SNR) along the lateral direction was calculated for each B-scan image at the depth of the horse hair. The calculated SNR values were plotted against the measured depths to estimate the maximum penetration depth. The slope of the SNR-to-depth curve determines the maximum imaging depth.

Fig. 6 (A) shows the schematic of the tissue phantom. A human hair was placed on top of the tissue surface to provide indication the location of the top surface in B-scans. In Fig. 6 (B), at the depth of 3 mm, the SNR is still higher than 15 dB, which demonstrated that the maximum imaging of PAM using a 50-MHz ultrasonic detector is more than 3 mm in this biological tissue.

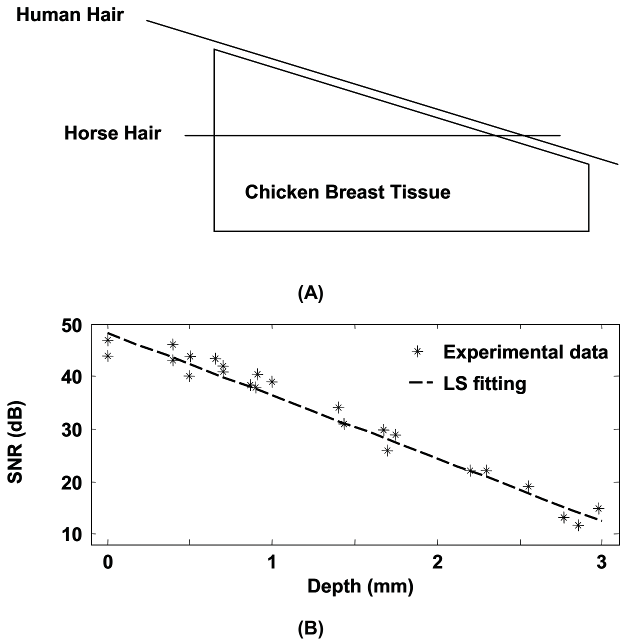

Fig. 6. PAM imaging of chicken breast tissue embedded with horse hair to measure the maximum imaging depth. (A) Schematic of the phantom. (B) Decrease of SNR with depth.

The 3-mm maximum imaging depth was further demonstrated in live animals (Fig. 7). A B-scan image of subcutaneous blood vessels was acquired from a dorsal side of a Sprague Dawley rat (~200 g, Charles River Breeding Laboratories, MA) *in vivo* without averaging (Fig. 7 (A)). The pointed vessels are ~0.7 mm below the skin surface. Then, in order to artificially increase the depth of the imaged subcutaneous blood vessels, a chicken breast tissue slab was used to cover the scanned area. A new B-scan of the same cross section was acquired without averaging, which is shown in Fig. 7(B). The vessels are now 3.3 mm below the top surface of the tissue slab and lower SNR is observed as expected. Fig. 7 (C) shows the image after a 40-time signal averaging, where improved SNR was achieved as anticipated.

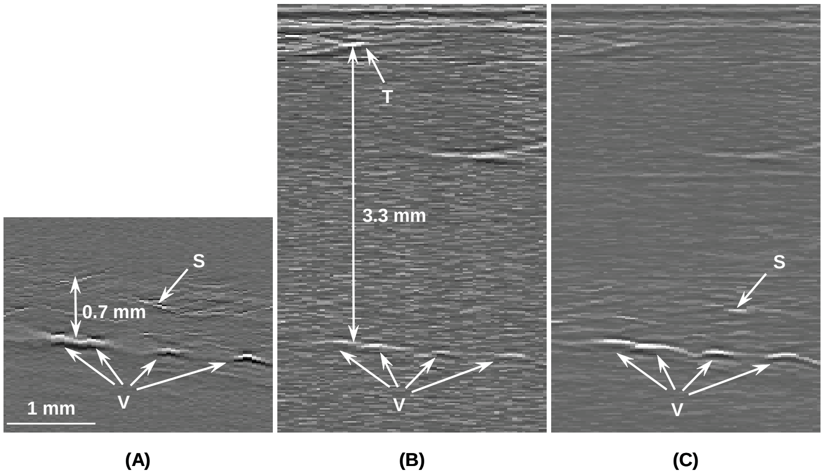

Fig. 7. An illustrative example showing the penetration depth of PAM in tissue. (A) B-scan image of subcutaneous vessels (B) B-scan image of the same vessels shown in panel A when the skin is covered by a chicken breast tissue slab. (C) B-scan image after 40-time signal averaging. S: skin surface; V: blood vessels; T: top surface of chicken tissue.

We have stated that both the spatial resolutions and the maximum imaging depth of PAM are scaleable with ultrasonic parameters within the reach of photons. An experimental result demonstrating such scalability is given in Fig. 8. In Fig. 8(A), the trend of increasing axial resolution with larger ultrasonic bandwidth is observed by imaging a 6-μm carbon fiber with 5 different ultrasonic transducers. In Fig 8(B), increasing imaging depth with lower central frequency is acquired for three ultrasonic transducers with central frequencies at 50 MHz, 30 MHz, and 25 MHz, respectively. When performing signal averaging for 40 times, the maximum imaging depth for the 25-MHz transducer was increased as a result of improved SNR.

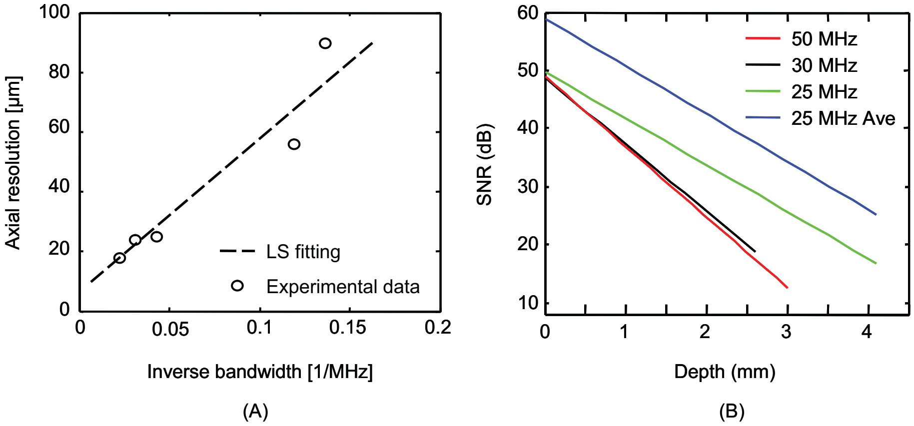

Fig. 8. Scalability of PAM. (A) Scalability of axial resolution with ultrasonic bandwidth. (B) Scalability of maximum imaging depth with ultrasonic central frequency. Ave: averaging.

CHAPTER III

STRUCTURAL PAM IMAGING IN ANIMALS

1. Image visualization

Since PAM images the optical absorption distribution in biological tissue in three dimensions, how to visualize such 3D data in order to best demonstrate the capabilities of PAM is important. We have used four different methods to visualize the acquired 3D images:

(1) B-scan image, *i.e.* cross-sectional image that is acquired from a single 1D scan along x-axis.

(2) Maximum-intensity-projection image (MIP),[48] where maximum PA amplitude of each A-line (along the z axis) is projected onto the x-y plane to form a 2D image after the skin signals are removed digitally. MIP images have been found suitable for visualizing the subcutaneous microvasculature.

(3) Multi-layered MIP images, where the acquired volumetric image is sectioned into several equally sized sub-volumes, and MIP image of each sub-volume is calculated individually. Compared with a simple total MIP, multi-layered MIP discloses depth information to some extent.

(4) Volume rendering[49] of the 3D data. This is the best visualization, which reveals both the depth information and the spatial orientations of blood vessels. However, it is computationally intensive, may have artifacts, and may ignore some tiny

structures with relatively low PA intensity. It requires high SNR and signal-to-background ratio, which may not always be possible.

There are some other visualization technologies that have already been established in the field of computer graphics, such as closest-intensity-projection, surface rendering, and cross-sectional image along arbitrary plane,[50] which are also applicable to PAM.

2. Imaging of subcutaneous microvasculature in rats

In biological tissue, oxyhemoglobin (HbO_2) and deoxyhemoglobin (HbR) are the dominating optical absorbers within a wide spectral range. Therefore PAM is highly sensitive to blood. Maslov *et. al.* have demonstrated, for the first time, the capability of PAM imaging of subcutaneous microvasculature in rats *in vivo*. In their work, the acquired MIP image was compared to a photograph taken from the dermal side of the scanned area after skin harvesting. Good agreement in the vascular anatomy and vessel branching between the PAM image and the photograph was observed. Since then, the optical illumination was modified to have a larger annular area and a better optical-ultrasonic alignment was achieved in PAM. A larger dark-field illumination reduced the optical energy density on both the skin surface and around the optical focus, and, moreover, a better illumination of the deep structures was achieved.

In this study, the *in vivo* imaging of subcutaneous blood vessels was conducted in a Sprague Dawley rat with a body weight of 200 g. The hair at the scanning area on the dorsal side was removed prior to data acquisition. A dose of 87 mg/kg Ketamine and 13 mg/kg Xylasine, was administered intramuscularly to anesthetize the rat, and supplemental injections (~50 mg/kg/hour) kept the rat motionless throughout the experiment. During the experiment, a Pulse Oximeter (8600 V, Nonin Medical, MN) was used to monitor the arterial blood oxygenation and heart rate; the body temperature was maintained throughout the experiment. All experimental animal procedures were carried out in conformity with the guidelines of the NIH.[51] The laboratory animal protocol for this work was approved by the University Laboratory Animal Care Committee of Texas A&M University.

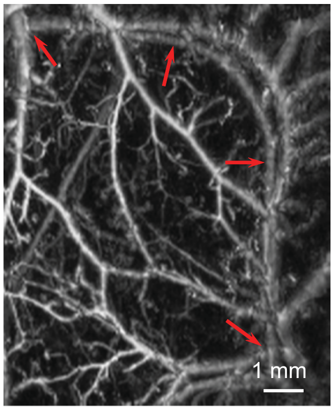

Fig. 9. PAM imaging of subcutaneous microvasculature in rats *in vivo.*

A volume of 10×8.2×3 mm^3 was scanned at the 584-nm optical wavelength at a step size of 50 µm. The MIP image was up-sampled 4 times using cubic spline interpolation method. The MIP result is shown in Fig. 9, where the signal-to-background ratio was 24±1.2 on average. The smallest vessel imaged has a diameter less than 50 µm, which is the step size of motor scanning. And up to 8 orders of vessel branching can be observed. However, due to the 0.3-mm focal zone of the ultrasonic transducer and the contour of the skin surface, there are regions that the targeted blood vessels were out of focus. Within those regions, degraded lateral resolution resulted in a blurred boundary and enlarged vessel diameters, which may cause wrong judgment based on such images.

3. Improvements of image quality

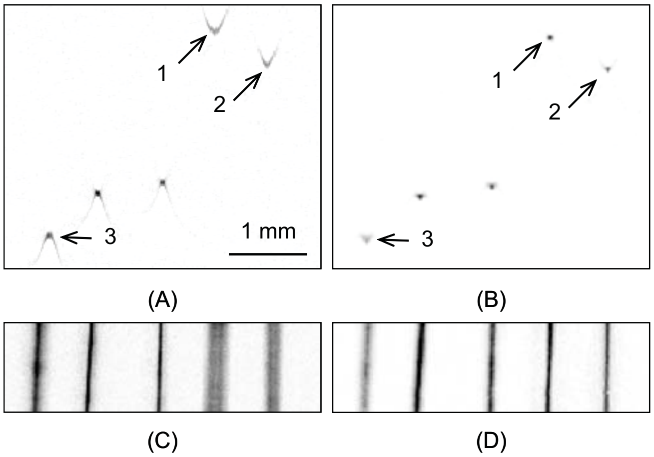

Fig. 10. Images of a carbon-fiber phantom. Two cross-sectional images are shown to demonstrate the depth-independent resolution before (A) and after (B) SAFT correction. The comparison of the MIP images before and after the SAFT correction is given by (C) and (D).

In order to have a correct representation of the volumetric morphology of the blood vessels, especially at those off-focus regions, a depth-independent lateral resolution must be achieved. Therefore, we employ a numerical method, referred to as virtual point-detector based synthetic aperture focusing technique (SAFT),[52] to compensate for the degraded off-focus lateral resolution. Based on phantom tests, both the lateral and axial resolutions are insensitive to the distance between the object and the surface of the ultrasonic detector after SAFT correction.

In a phantom test, five carbon fibers with a diameter of 6 μm were placed at different heights within a range of 2 mm in an optical scattering solution to mimic micro blood vessels in biological tissue. A volume of 1×4×3 mm^3 was imaged with a 20-μm scanning step. Due to the 0.3-mm focal zone, some carbon fibers were out of the focal region and, as a result, degraded lateral resolution was observed. Then, SAFT was applied to correct the degraded lateral resolution at the locations out of the focal region.

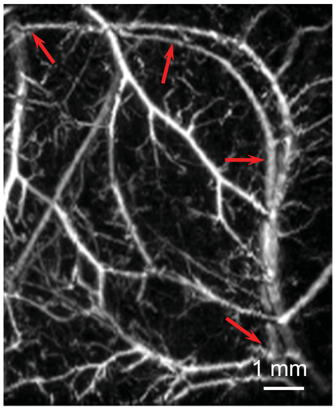

Fig. 11. *In vivo* PAM imaging of subcutaneous microvasculature in rats after SAFT correction.

Figure 10 shows the carbon-fiber phantom results in two dimensions. Fig. 10(A) and Fig. 10(B) are typical cross-sectional images before and after SAFT correction. In Fig. 10(B), the fibers marked 1, 2 and 3, which are strongly degraded in Fig. 10(A), have been corrected to a size that is comparable to those around the focal region. Fig. 10(C) and Fig. 10(D) are MIP images, where the comparison of the degraded lateral resolution and correction is better demonstrated. This phantom study proves that depth-independent spatial resolution, which is critical for the complete 3D imaging of blood vessels, can be achieved.

Figure 11 shows the image after SAFT correction using the *in vivo* data that is shown in Fig. 9. The blurred vessels pointed out in Fig. 9 are now corrected, to some extent, and the anatomical structures are better revealed. Due to the motion artifacts, only 1D SAFT correction was performed along the *x*-axis.

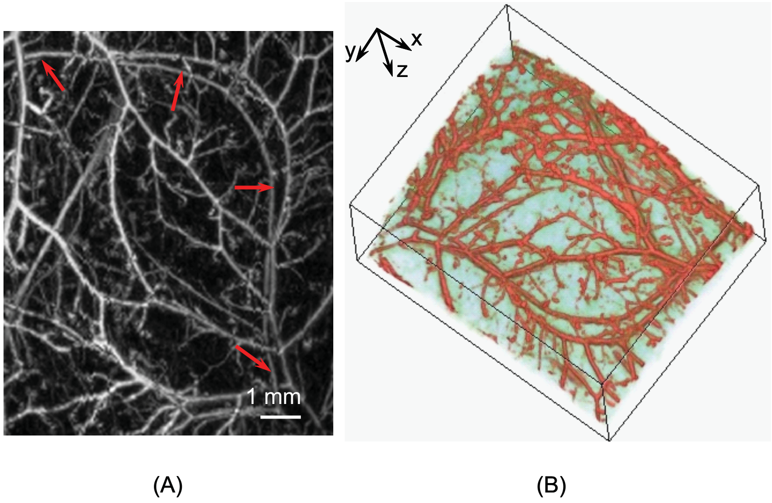

Fig. 12. *In vivo* PAM imaging of subcutaneous microvasculature in rats based on auto-fit scan. (A) MIP image. (B) 3D image based on volume rendering.

To further improve the image quality, an auto-fit scanning mode was developed for PAM. Based on the anatomical observation, the subcutaneous vasculature in rats are mainly located within a short depth range from the skin surface. Therefore, we can adjust the distance between the ultrasonic transducer and the skin surface so that the layer of vessels is always within, or not far from, the ultrasonic focal zone. To do that, a normal flat scan was performed first. Then the location of the skin surface was detected. One location in the *x*-*y* plane, where the best focusing of the vessel layer was observed, was chosen as the origin point along the *z* axis. And the distance to the origin point along the *z* axis was calculated at each transducer location and was further converted to motor steps. Finally, the motor controlling program adjusted the vertical position of ultrasonic transducer to follow the skin contour. The disadvantage of auto-fit is that it requires twice the data acquisition time.

Figure 12 shows the result from an auto-fit scan. Compared with the result from a normal flat scan and SAFT correction, the best image quality has been achieved. In Fig. 12(A), all the vessels, which were located at off-focus regions previously, were imaged with the best lateral resolution around the focal zone. More details of the tiny vessels, where are not clearly observed in Fig. 9 and Fig. 11 are now clearly observed. Fig. 12(B) gives a 3D volume rendering result in pseudocolors, where the 3D image acquired from an auto-fit scan were further corrected by SAFT and the original location of the vessels were recovered based on the detected skin location. In Fig. 12(B), vessels that are located at different depth from the skin surface and that have different spatial orientations are clearly visualized.

4. Imaging of angiogenesis in rats

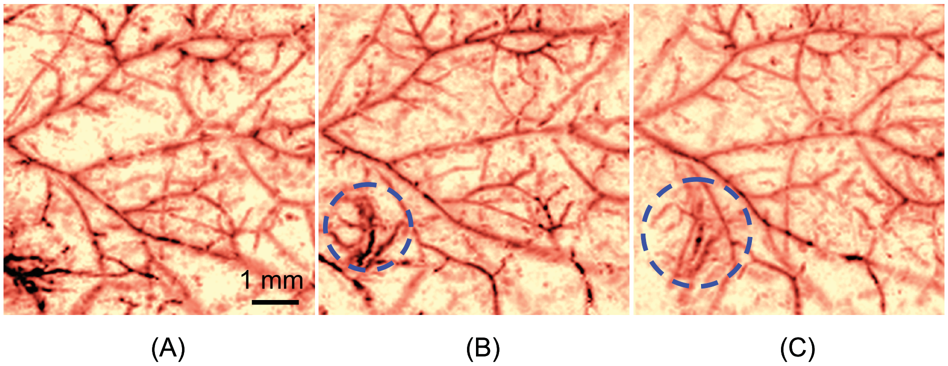

Fig. 13. Images of tumor angiogenesis *in vivo* by PAM at (A) before, (B) two days post, and (C) five days post subcutaneous inoculation.

Owing to its high spatial resolution and high contrast in imaging blood vessels, PAM can be used to monitor angiogenesis. Imaging of angiogenesis is invaluable for understanding tumor growth and metastasis because blood vessels feed the tumors with nutrients for growth and circulate tumor cells from their primary site during metastasis.[53] High-quality angiogenesis imaging can provide quantitative measures such as intratumoral microvessel density (MVD) and vessel spacing for both diagnosis and prognosis. Furthermore, imaging of angiogenesis is desirable in evaluating cancer treatment, *e.g.*, assessing the efficacy of angiogenesis inhibitors. As yet only Doppler OCT has the potential to image microvasculature with high spatial resolution.[54,55] Although significant results have been achieved using confocal microscopy, or multiphoton microscopy, on cancer specimens, none of the existing methods are capable of imaging the microvasculature of tumors in their natural environments *in vivo* without using an extrinsic contrast agent.

In this *in vivo* monitoring of tumor angiogenesis, five million brain metastatic rat mammary adenocarcinoma cell (BR_7C_5) was subcutaneously inoculated in a 200-g Sprague Dawley rat to develop tumor. Images of the tumor were acquired at the isosbestic optical wavelength of 584 nm at three different time points (before, two days post, and five days post inoculation). The tumor was invisible from the skin surface with unaided eyes.

Figure 13 shows the results of the angiogenesis imaging. The mean depth of the imaged vessels is 0.72±0.17 mm from the skin surface, with a maximum depth of 1.7 mm. The image in Fig. 13(A) was taken before the inoculation, which serves as a baseline. The image taken at two days post inoculation shows new vessels with an irregular architecture and blurry boundaries as circled in Fig. 13(B). Loss of vascular symmetry and irregularity relative to those of the adjacent normal vascular structures indicates the location of tumor angiogenesis within an area 2 mm in diameter. The image taken at five days post inoculation (Fig. 13(C)) shows that the angiogenic area has expanded. With the growth of the tumor, the vessel boundaries have become clearer as shown in Fig. 13(C). In Fig. 13(B) and Fig. 13(C), more complexity and a higher MVD of the tumor vasculature in the inoculation region is distinguishable from the surrounding healthy vessels. In the PAM images, the smallest cancerous vessel observed has the diameter about 50 µm within an area of 2 mm in diameter. In comparison, the minimal tumor that current techniques can detect in most clinical cases is 1 cm in diameter. Although PAM is not yet capable of imaging angiogenesis at the capillary level, it detects tumor angiogenesis at the stages earlier than any other clinical modality do. Since MVD is a *bona fide* predictor of aggressive tumor growth and metastasis,[56] PAM can potentially detect angiogenesis in the early stage of tumor development and monitor anti-angiogenesis therapy temporally and, consequently, improve patients' chance for cure and survival.

5. Imaging of acute skin burn in pigs

The extent and depth of burn injury are the two most important parameters for the clinical evaluation of burns.[57] Burn wounds are categorized by depth into superficial, partial-thickness and full-thickness burns. With both very shallow (superficial, 0.07~0.12 mm) and very deep (full-thickness, >2 mm) burns, clinical assessment of the burn depth is generally accurate. However, the most complicated cases are partial-thickness burns, which range from 0.12 mm to 2 mm and are further divided into superficial partial-thickness and deep partial-thickness burns. Owing to the destruction of the epidermis and a portion of the underlying dermis, clinical decisions about partial-thickness burns are difficult to make and often inaccurate.[58,59] Because superficial partial-thickness burns heal well without surgical intervention while deep partial-thickness burns require immediate medical attention or skin grafting, there is a need for accurate determination of burn depth by noninvasive technologies.

Existing techniques that can measure burn depth noninvasively include laser Doppler perfusion imaging (LDPI),[60] polarization sensitive optical coherence tomography (PSOCT),[61,62] indocyanine green dye fluorescence,[63] thermography, ultrasound, and nuclear magnetic resonance imaging. Among these techniques, LDPI has drawn the most attention, and PSOCT is considered to have the most potential for the quantitative estimation of actual burn depth.

LDPI detects the reduced blood flow that results from damaged dermal vasculature in order to estimate depth through a two-dimensional mapping of blood perfusion. However, because it uses a laser with a long coherence length, LDPI cannot provide depth resolved information, and the correlation between the perfusion value and the burn depth is not straightforward. Moreover, LDPI is seriously affected by the optical heterogeneity of tissue. PSOCT measures the depth directly by acquiring cross-sectional images of thermal injuries with high spatial resolution. It images the optical polarization changes in tissue that result from the thermal destruction of collagen fibers. But because PSOCT detects only the direct-reflected (singly backscattered) photons, its imaging depth in biological tissues is fundamentally limited to less than 1 mm due to strong optical scattering. This depth limit makes PSOCT unsuitable for imaging partial-thickness burns that are deeper than 1 mm. Consequently, a new noninvasive technique that provides high-resolution depth-resolved imaging of burns at a depth of a few millimeters offers great promise.

PAM measure the burn depth based on imaging the hyperemia of acute thermal injuries, which has increased optical absorption than the healthy and thermally coagulated tissues due to higher blood content.[64,65] In contrast to LDPI, PAM provides high-resolution depth-resolved imaging. In contrast to PSOCT, PAM can image deeper to cover the whole range of partial-thickness burn. Based on this effect, the feasibility of using PA profiling to evaluate burn depth has been demonstrated in rats. However, only poor spatial resolution has been achieved.[66,67]

We used the White Yorkshire pigs (20~30 kg) with low skin melanin concentration as our animal model because pig skin has the closest anatomical resemblance to human skin.[68] After anesthetizing the animal with an intramuscular injection of xylazine at a dosage of 2.2 mg/kg and Telazol at a dosage of 5 mg/kg, an area of 10×10 cm^2 on the pig back was depilated with commercial hair removing lotion. An acute burn was created by applying an electric cautery (Thermal Cautery Unit 150, Geiger Medical Technologies, IA; preheated to 175 ^{o}C) to the depilated skin area. After heating, edema and tissue coagulation were observed without obvious carbonization. A series of acute burns with different depths of damage were inflicted by varying the skin exposure to the cautery that was preheated to 150 ^{o}C. During each heating period, we tried to maintain the pressure applied to the skin through the cautery. However, it has been found that the burn depth is insensitive to such pressure. The burned skin together with a large area of adjacent normal skin and subcutaneous tissues were immediately excised to a depth of 10 mm for PAM imaging. After the skin excision, the animals were euthanatized by an intravenous administration of pentobarbital at a dosage of 100 mg/kg. All of the burns were classified by histological analyses as deep partial-thickness burns.

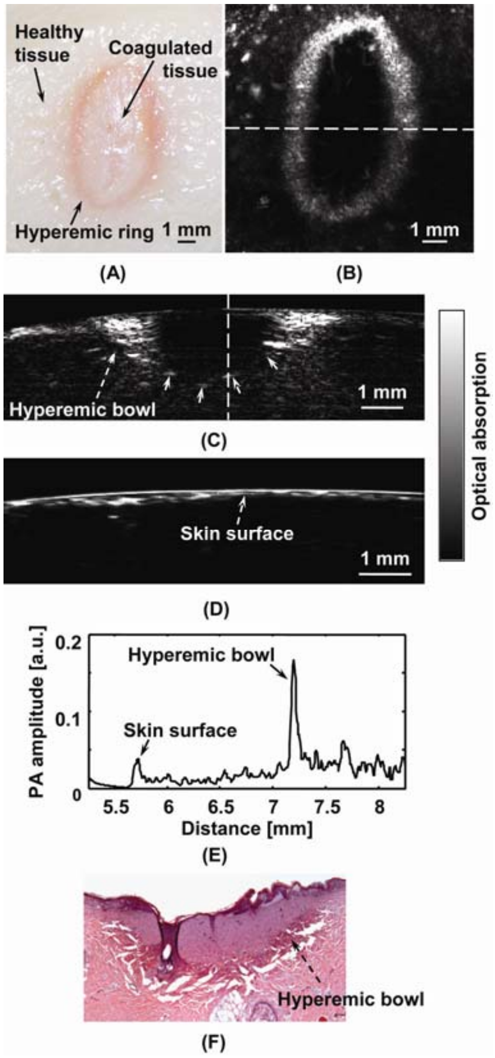

Fig. 14. PAM image of an acute skin burn heated at 175 ^{o}C for 20 s. (A) A photograph of the burn from the epidermal side. (B) A MIP image showing the morphology of the hyperemic ring. (C) The B-scan image of the hyperemic bowl at the location marked in panel B. (D) A typical B-scan image of healthy skin. (E) The A-line at the location marked in panel C. (F) A haematoxylin-and-eosin (HE) stained histological section.

Figure 14 (A) shows a photograph of an acute skin burn that was heated at 175 ^{o}C for 20 s, which was taken from the epidermal side after skin excision. A volume of 10×10×3 mm^3 that covered the burn injury was imaged by PAM. Due to the optical and strong acoustic attenuations, the acquired PA signals from the hyperemic bowl on skin surface had a much higher amplitude than those from below. Therefore, the MIP image (Fig. 14(B)) shows only the hyperemic ring on the skin surface. For B-Scan images, amplitude compensation was applied to better visualize the deeper structures. Since the acoustic attenuation is the dominating factor at a 50-MHz central frequency, the measured PA amplitudes at difference depths beneath the skin surface were compensated for based on the acoustic attenuation in porcine skin (2.5 dB/cmMHz).[69] This compensation provided a good first-order estimation of the real values for structural imaging purposes. After being compensated for, the B-scan image of the burn at the marked location in Fig. 14(B) is given in Fig. 14(C). For comparison, a B-scan image of an untreated healthy skin is given in Fig. 14(D).

Based on the pathological studies, a typical acute thermal injury consists of three distinct regions: (1) a central white zone of edema and coagulated tissue, where no blood flow is expected; (2) a red band called hyperemic bowl (hyperemic ring when on the skin surface,) which is resulted from hemorrhage at the periphery of the coagulated zone; and (3) the outside thermally intact healthy tissue area.[70] These three zones are clearly observed in Fig. 14(A). Because PAM is an optical absorption based imaging modality and hemoglobin is the dominant optical absorbing pigment at the 584-nm wavelength, the contrast in PAM imaging of acute burn comes from the differences in hemoglobin concentration. Although increase in optical scattering in the coagulated tissues than the healthy tissues has been found, the optical absorption of the coagulated tissue remains relatively the same around the 584-nm wavelength. For edema, both the optical scattering and absorption are decreased comparing with those of normal tissues.[71] As a result, the hyperemic bowl generated stronger PA signal than the healthy and thermally coagulated tissues due to higher hemoglobin concentration. In Fig. 14(B), the ratio of the imaged PA amplitude of hyperemic ring to that of the inner coagulated tissue was 20.4±3.4; and the ratio of the imaged PA amplitude of hyperemic ring to that of the outer normal tissue was 9.5±1.9. Compared to the photograph shown in Fig. 14(A), both the morphology and the size of the hyperemic ring were correctly imaged by PAM.

In Fig. 14(C), the middle dark region represents the thermally coagulated tissue, whose boundary is defined by the brighter hyperemic bowl as pointed by the arrows. Because capillaries were beyond the spatial resolution of current PAM system, no obvious structures were imaged in the outside healthy tissue in this burn sample. A typical B-scan of a normal healthy skin is given in Fig. 14(D) for comparison. Although the compensation for the acoustic attenuation may cause possible artifacts in burn imaging, the same attenuation compensation was applied to healthy skin imaging and no artifact was found so far.

Once the B-scan image of the hyperemic bowl was acquired, the burn depth was estimated based on the distance between the imaged skin surface and the inner boundary of the hyperemic bowl. Fig. 14(E) gives the A-line at the location marked in Fig. 14(C), where the x-axis is the distance from the ultrasonic transducer. The two PA peaks in the

A-line correspond to the skin surface and the inner boundary of hyperemic bowl, respectively. Thus the distance between these two peaks was considered as the burn depth. After a lateral neighborhood averaging within a region of 0.5 mm along the *x* axis, the maximum burn depth in Fig. 14(C) was measured to be 1.73±0.07 mm.

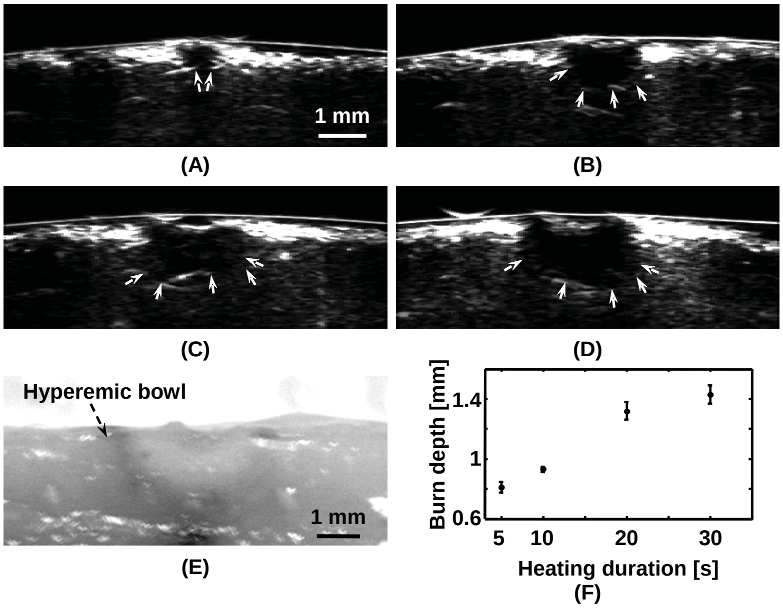

Fig. 15. PAM imaging of acute skin burns with different depths introduced by changing the durations of heating for 5 (A), 10 (B), 20 (C), and 30 (D) seconds. A photograph of the cross section shown in panel D is given in (E), and the imaged change of burn depth with heating duration is given in (F).

Figures 15 (A)-(D) show the B-scan images of the acute skin burns that were heated at 150 ^{o}C for 5, 10, 20, and 30 s, respectively. Increasing burn depth was observed for longer thermal exposure according to the imaged inner boundaries of the hyperemic bowls, which agreed with the pathogenesis of acute burns. Moreover, the imaged width of the hyperemic bowls on the skin surface also increases with longer heating, which was proven by the observation before skin excision. The photograph in Fig. 15(E) shows the same cross section as shown in Fig. 15(D) of the 30-s burn. Both the imaged width and depth of the hyperemic bowl fit the observations from the photograph. The measured maximum burn depth versus the heating duration is given in Fig. 15(F), where the trend of increasing burn depth is further demonstrated. In this special case, PSOCT was found not applicable to a burn with heating duration longer than 10 seconds.

The hyperemic bowl representing the area in which hemostasis, hemorrhage, and hyperemia occurred as a result of thermal damage to the blood vessels and as a pathophysiologic response to the heating, which marked the boundary of the thermal damage. Comparing with the LDPI and the PSOCT that need to correlate the measured parameters, such as blood perfusion and polarization change, to the actual burn depth, PAM provides a direct assessment of the true boundary of the burn by imaging the hyperemic bowl. Because the vascular damage has been found to be a much more sensitive indicator of burn assessment than the parenchymal changes, such as denatured collagen, PAM has the potential to have high accuracy in assessing burn depths. PAM is not sensitive to edema because it introduces only small optical absorption changes relative to the strong optical absorption of hemoglobin. Since the imaged burn depth measures up to 1.73±0.07 mm, PAM is well suitable for imaging human skin. Therefore

PAM has the potential to play an important role in clinical burn diagnosis, treatment and prognosis. However, some exceptions may exist in the post acute burns and some slow burns, where the boundaries of the thermal damages may not be well defined by the hyperemic bowl due to reasons such as cellular infiltrates.

In this study, acute burns were imaged immediately after the thermal exposure using a single optical wavelength at the isobestic point. To better understand the pathophysiology of the burn injuries, the hemoglobin oxygen saturation could be measured using multi-wavelength PAM imaging. The time course study of the change of hemoglobin oxygen saturation could be conducted to investigate the post burn reactions and to examine the healing procedure.[72]

There are two technical limitations in the current PAM. First, due to low laser repetition rate (10 Hz) data acquisition for one B-scan image (20 times averaging) takes about 10 minutes. Motion artifacts during this period could affect the accuracy of the depth measuring in *in vivo* studies. To solve this problem, a new system with a laser repetition rate up to 1 kHz is under construction and the data acquisition time will be reduced significantly. The second limitation is that PAM requires a coupling medium between the ultrasonic detector and damaged tissues in order to detect the induced PA waves. This contact may create some difficulties in the clinical environments. However, no pressure was applied through the coupling medium and sterilized ultrasound gel, which is commercially available, can be used to prevent infections.

6. Imaging of skin melanoma in mice

All the structural imaging results presented above are based on a single optical wavelength targeting at the blood vessels. By extending single-wavelength imaging to dual-wavelength imaging, PAM can separate the contributions from various pigments based on their unique molar extinction spectra. A good example that has potential clinical importance is melanoma imaging.

Knowledge of the depth of invasion and 3D shape of malignant melanoma is critical to clinical decision and prognosis. Especially, depth and thickness of melanoma guide the choice of treatment. The current clinical practice is based on invasive excisional or incisional biopsies, which causes not only pain but also potential damages to nearby healthy skin. Noninvasive imaging methods have the potential to alleviate such problems, and also allow physicians to monitor it during treatment.

Several technologies have been explored as possible noninvasive melanoma imaging methods. However, they suffer from critical limitations. Epitherial illumination microscopy and confocal scanning laser microscopy offers insufficient penetration depth to measure the thickness of melanoma. High frequency sonography has long penetration depth, but the image has a poor contrast. In terms of ultrasound, melanoma is homogeneously echo-poor in comparison with echo-rich dermis, from which it can be distinguished. As a result, PAM has the advantages to provide larger imaging depth than epitherial illumination microscopy and confocal microscopy; and to provide higher spatial resolution and higher imaging contrast than high frequency sonography.

In this work, 3D morphology of subcutaneous melanoma and nearby vascular system were imaged. We imaged a subcutaneously inoculated B16 melanoma in an immunocompromised nude mouse (body weight: 20 g). Two optical wavelengths (584 and 764 nm) were used in this experiment. Using the 584-nm optical wavelength, PAM can image the morphological relationship between a melanoma tumor and the surrounding blood vessels in the *x-y* plane because of the comparably strong absorption of both melanin and hemoglobin in this spectral region. However, visible light cannot be used to evaluate the tumor thickness because it cannot penetrate through the melanin-rich tumor. To compensate for this limitation, PAM works in the near-infrared spectral region as well, where light can infiltrate the tumor due to the decreased absorption of melanin and the minimal absorption of blood. The combination of two images from these two spectral regions reveals the 3D morphology of both the melanoma and its surrounding vasculature as shown in Fig. 16, where some parallel arterioles and venules are evident.

From a photograph (Fig. 16 (A)) taken from the epidermal side, no tumor morphology or vessel structure is clearly observed. A composite of the two MIP images projected along the *z* axis, where blood vessels are pseudo-colored red in the 584-nm image and the melanoma is pseudo-colored brown in the 764-nm image is given in Fig. 16(B), where micro vessels, presumably, resulting from angiogenesis, are observed clearly surrounding the tumor. As many as six orders of vessel branching can be observed in the image as indicated by numbers 1-6. Fig. 16 (C) shows a 3D rendering of the melanoma acquired at the 764-nm wavelength. Two MIP images at this wavelength projected along the *x* and *y* axes are shown on the two side walls, respectively. The composite image shown in panel A is redrawn at the bottom. The top surface of the tumor is 0.32 mm below the skin surface, and the thickness of the melanoma is 0.3 mm. An enlarged B-scan image of the melanoma parallel with the *z*-*x* plane at the location marked with a dashed line in Fig. 16(A) is given in Fig. 16(D). For comparison, a HE stained section at the same marked location is shown in Fig. 16 (E).

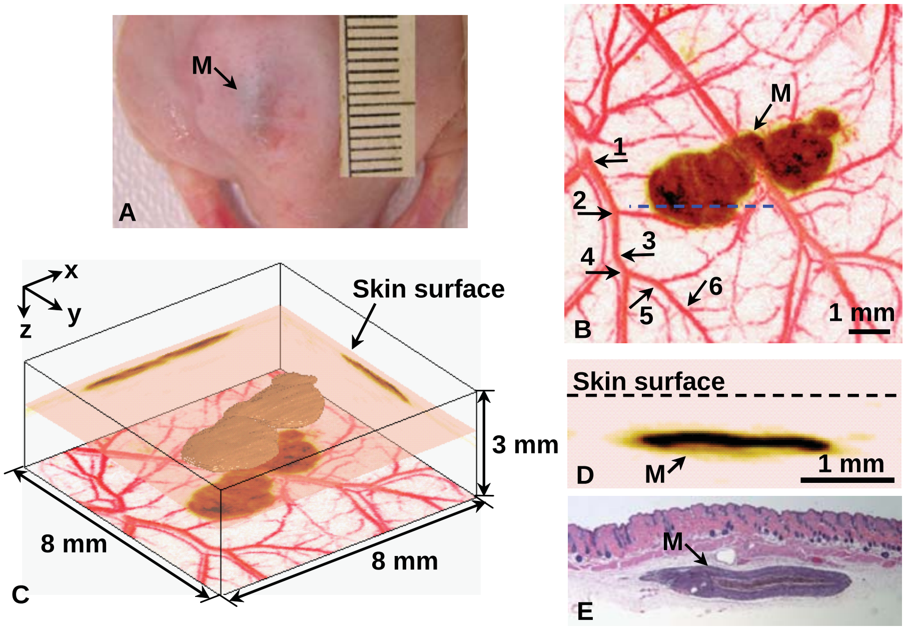

Fig. 16. Images of a melanoma in a nude mouse *in vivo.* (A) Photograph of the melanoma tumor. (B) A composite MIP image. (C) 3D rendering of the melanoma. (D) An enlarged B-scan image of the melanoma. (E) HE stained section. M: melanoma.

In this study, at the 584-nm wavelength, the average ratio of the vessel to the background in PA signal amplitude is 13±0.89, and the average ratio of the melanoma tumor to the surrounding blood vessels is 0.92±0.02. However, at the 764-nm wavelength, the average ratio of the melanoma tumor to the blood vessels is 29±3, and the average ratio of the melanoma tumor to the background is as high as 68±5. The contrast-to-noise ratio for melanoma is 67 dB and 64 dB on average at the 584-nm and 764-nm wavelengths, respectively, where the major noise is thermal noise. A composite volumetric visualization is given in Fig. 17.

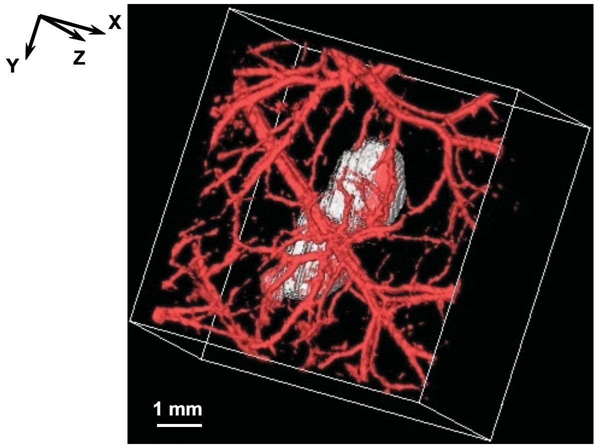

Fig. 17. Volumetric imaging of a melanoma tumor and its surrounding blood vessels *in vivo*.

Such high optical contrast and specificity are due to the strong absorption of both hemoglobin and melanin and the minimal background absorption. This result demonstrates that PAM can potentially be used to provide critical information for the clinical diagnosis and prognosis of melanoma as well as for the evaluation of melanoma progression and treatment. By choosing optical wavelengths targeted at other endogenous pigments or administered chemical compounds, PAM can be easily adapted to other applications.

CHAPTER IV

FUNCTIONAL PAM IMAGING IN SMALL ANIMALS

1. Introduction

Functional imaging of small animals, such as rats and mice, is a vital tool in the study of various diseases. Noninvasive, quantitative, and repetitive imaging of biological processes in living animals changes the way in which many experiments, in modeling of human diseases and normal physiological processes, are conducted. Animal models of human diseases, such as cancers and Parkinson's disease, are providing critical information about the causes, diagnosis, and therapy of these diseases; and are offering us the opportunity to evaluate pathologic progressions in much-compressed time frames.

Among many functional parameters, hemoglobin oxygen saturation (SO_2) is of great importance and has drawn many attentions. Imaging SO_2 is important for understanding brain hemodynamics in response to sensory stimulations.[73] It is also invaluable for numerous medical applications, such as evaluating the effects of chemotherapy and radiotherapy on tumors,[74] monitoring the healing of wounds, and studying gene expression.[75] However, SO_2 has not been routinely imaged due to the existing noninvasive methods' lack of either spatial resolution or sensitivity. Current techniques that show potential for SO_2 imaging include near-infrared spectroscopy (NIRS),[76] blood oxygen level-dependent (BOLD) contrast MRI,[77] electron paramagnetic resonance imaging (EPRI),[78] PET, and SPET.[79] NIRS measures diffuse light at different wavelengths and calculates the SO_2 based on spectral measurements and the molar extinction differences between HbR and HbO_2. However, it suffers from poor spatial resolution because of the strong optical scattering in biological tissue. Although BOLD MRI can provide high spatial resolution, it is only sensitive to HbR and has trouble distinguishing between changes in oxygenation levels and changes in blood flow. Because it is unable to image intrinsic contrast, EPRI requires the injection of potentially toxic free-radical contrast agents. PET and SPET require the intravenous administration of radioactive isotopes, and both have poor spatial resolution.

As aforementioned, PAM is well suited to the imaging of blood vessels within an appropriate spectral region. Based on only endogenous contrast, PAM can reach a signal-to-background contrast of 3,500% with high sensitivity and specificity *in vivo*. As a result, PAM provides better spatial resolution than NIRS by taking advantage of ultrasonic detection, and it provides higher sensitivity than MRI due to high physiologically specific optical absorption contrast.

PAM measures SO_2 in the same way as does NIRS,[80] where HbR and HbO_2 are treated as the dominant absorbing compounds at each wavelength (λ_i). Thus the blood absorption coefficient $\mu_a(\lambda_i)$ (cm^{-1}) can be expressed as

$$\mu_a(\lambda_i) = \varepsilon_{\mathrm{HbR}}(\lambda_i)[\mathrm{HbR}] + \varepsilon_{\mathrm{HbO_2}}(\lambda_i)[\mathrm{HbO_2}], \tag{4.1}$$

where $\varepsilon_{\mathrm{HbR}}(\lambda_i)$ and $\varepsilon_{\mathrm{HbO_2}}(\lambda_i)$ are the known molar extinction coefficients ($\mathrm{cm}^{-1}\ \mathrm{M}^{-1}$) of HbR and HbO_2 at wavelength λ_i, respectively; and $[\mathrm{HbR}]$ and $[\mathrm{HbO_2}]$ are the concentrations of the two forms of hemoglobin, respectively. Since the amplitude of the acquired localized PA signal $\phi(\lambda_i, x, y, z)$ is proportional to the localized optical energy absorption, we can replace the $\mu_a(\lambda_i)$ by $\phi(\lambda_i, x, y, z)$ to calculate the $[\mathrm{HbR}]$ and $[\mathrm{HbO_2}]$ in relative values. Least-squares fitting gives

$$\begin{bmatrix}[\mathrm{HbR}]\\ [\mathrm{HbO_2}]\end{bmatrix}_{(x,y,z)} = \left(M^T M\right)^{-1} M^T \Phi(x,y,z) K\,, \tag{4.2}$$

where $M = \begin{bmatrix}\varepsilon_{\mathrm{HbR}}(\lambda_1) & \varepsilon_{\mathrm{HbO_2}}(\lambda_1)\\ \vdots & \vdots\\ \varepsilon_{\mathrm{HbR}}(\lambda_n) & \varepsilon_{\mathrm{HbO_2}}(\lambda_n)\end{bmatrix}$, $\Phi(x,y,z) = \begin{bmatrix}\phi(\lambda_1, x, y, z)\\ \vdots\\ \phi(\lambda_n, x, y, z)\end{bmatrix}$, and K is the proportionality coefficient that is related to the ultrasonic parameters and the wavelength-dependent change of the local optical fluence as light passes through the skin.[43,81] Thus, the dimensionless SO_2 is calculated as

$$\mathrm{SO}_{2(x,y,z)} = \frac{[\mathrm{HbO_2}]_{(x,y,z)}}{[\mathrm{HbO_2}]_{(x,y,z)} + [\mathrm{HbR}]_{(x,y,z)}}\,. \tag{4.3}$$

Due to the unknown coefficient *K*, only relative concentrations of the HbR and HbO_2 are calculated from (4.2). However, the SO_2 from (4.3) is an absolute measurement. Although two wavelengths are enough to determine SO_2 in principle, we used four wavelengths in all of our studies in order to reduce the influence of measurement error. The spectral region was between 570 nm and 600 nm, where a high optical absorptive contrast between the blood and the surrounding tissue, as well as minimal inversion error, could be achieved. The published molar extinction coefficients[82,83] of HbR and HbO_2 were used in both the *ex vivo* and *in vivo* experiments.

2. System tests

Prior to the *in vivo* study, the PAM system was tested by (1) calculating the concentration fraction of red ink in double-ink (blue and red inks) solutions, and (2) comparing the SO_2 values from PAM measurements with values acquired by a standard optical method using bovine blood samples *ex vivo*.

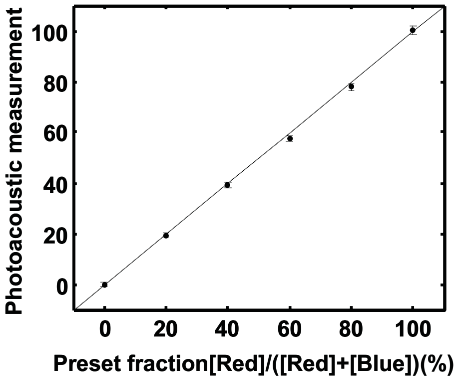

Fig. 18. PAM measurements of the fraction of the red ink concentration in a mixture of red and blue inks.

In the phantom study, two ink samples (Fiesta Red and Lake Placid Blue, Private Reserve Ink, IN) were mixed in various concentration ratios to mimic different levels of SO_2. By controlling the total concentration, the mixed samples had optical absorption coefficients comparable to that of blood. The four optical wavelengths in this study were 570 nm, 580 nm, 590 nm, and 600 nm. During data collection, the mixed solution was injected into a transparent tube (TYGON S-54-HL, Norton Performance Plastics, NJ) with an inner diameter of 0.25 mm. The fraction of the red ink concentration in the total ink concentration, [Red]/([Red]+[Blue]), was calculated using the peak PA amplitude measured by PAM, which matched the actual values with less than 1% error. The comparison between the calculated values and the true values are given in Fig. 18.

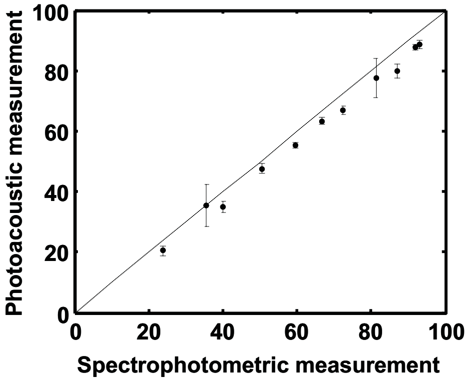

Fig. 19. Comparison of PAM measurements with spectrophotometric measurements of SO_2 in *ex vivo* bovine blood samples.

In the *ex vivo* bovine blood study, venous blood was freshly acquired and was mixed with anticoagulant (citrate dextrose solution) before the experiment. Oxygenated and deoxygenated bloods were obtained by saturating the blood with pure oxygen and pure carbon dioxide, respectively. Then, the fully oxygenated and deoxygenated bloods were mixed in different volumetric ratios to make samples of various SO_2 levels.[84] These samples were injected into the transparent tube and PAM measurements were made at four optical wavelengths: 578 nm, 584 nm, 590 nm, and 596 nm. During the experiment, a slow and steady blood flow (~0.4 ml/hr.) inside the tube was maintained by an infusion pump (A-99, Braintree Scientific, MA).

In addition to the PAM measurements, the SO_2 levels of these blood samples were also measured using a spectrophotometric method for comparison.[85] The mixed blood samples were first hemolyzed by adding 0.5% saponin. Then the optical absorption of each sample was measured by a spectrophotometer (GENESYS 20, Thermo Electron, MA) with near infrared light (from 700 nm to 1000 nm with a step size of 4 nm) to calculate SO_2. These two independent calculations of SO_2 agreed with each other with a systematic disagreement level of ~4% (Fig. 19), which presumably came from the optical scattering in blood and different readings of optical wavelengths in the two systems, but could be compensated for by a system calibration. The mean standard error of the PAM results was only 0.2%, which indicates the high sensitivity of PAM in measuring SO_2. In conclusion, the ink phantom and the bovine blood studies proved the high accuracy and sensitivity of PAM for the quantitative imaging of SO_2.

3. Static SO_2 imaging

In vivo data were collected on Sprague Dawley rats (body weight: 200 g) for both static and dynamic SO_2 imaging. Only MIP images are used here to visualize the final results.

Before imaging, hair was removed from the back of rats with a commercial human hair remover. A dose of 87 mg/kg Ketamine, plus Xylasine 13 mg/kg, was administered intramuscularly to anesthetize the rat and supplemental injections (~50 mg/kg/hour) kept the rat motionless throughout the experiment.

Four wavelengths (578, 584, 590, and 596 nm) were employed sequentially to acquire four different images. Fig. 20(A) shows the structural MIP image of subcutaneous vessels, which was acquired at the 584-nm wavelength. Since HbR and

HbO_2 have identical molar extinction coefficients at this optical wavelength (isosbestic point), Fig. 20(A) reflects the total hemoglobin concentration distribution.

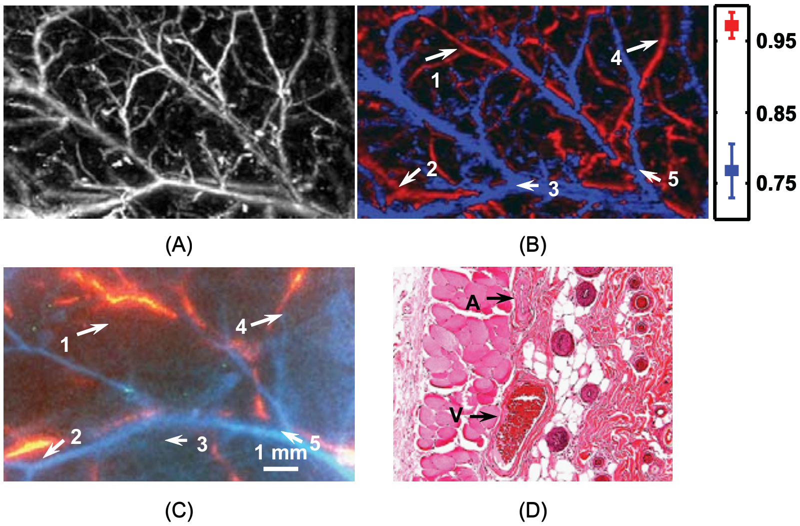

Fig. 20. Vessel-by-vessel imaging of static SO_2 *in vivo*. (A) A structural image acquired at the 584-nm optical wavelength. (B) A vessel-by-vessel SO_2 mapping. (C) A blood-perfusion image showing the arterioles (red) and the venules (blue). (D) HE-stained section showing the vessel structure at the location marked with a dashed line in panel C.

Based on anatomical observation after the *in vivo* experiment, the imaged blood vessels were located beneath the dermis. The wavelength-dependent optical attenuation in the dermal layer must be considered in imaging SO_2. In this study, the measured PA amplitudes were compensated for, by the average wavelength-dependent optical attenuation, which was acquired by measuring the PA amplitudes generated from a subcutaneous implant of black polyethylene film at different optical wavelengths. This average optical attenuation spectrum of dermis has been shown not to change significantly with different imaging locations and animals.

After images were acquired at all four different optical wavelengths at each physiological state, the $[HbR]$ and $[HbO_2]$ were first calculated on a point-by-point basis, and then the SO_2 was calculated within the blood vessels only, based on a vessel segmentation from the structural image. Because the SO_2 levels of venous and arterial bloods are physiologically distinctive, arterioles and venules can be separated based on the imaged SO_2 values

Figure 20(B) gives a vessel-by-vessel SO_2 mapping based on a least-squares fitting of the four images. The calculated SO_2 values are shown in the color bar, which measured around 0.97±0.02 in arterial blood and 0.77±0.04 in venous blood. The PAM imaged SO_2 values agree with systemic literature values.[86] While all other techniques measure volume-averaged SO_2, PAM provides a vessel-by-vessel mapping of SO_2.

In order to provide proof of the separation of venules and arterials, a blood-perfusion study was conducted as shown in Fig. 20(C). The perfusion study was modified from the traditional ink-and-gelatin procedure[87] by replacing the stained gelatin solution with a 1-ml suspension of 20-mg red-fluorescent microspheres (Fluorscent Polymer Microsphere, Duke Scientific, CA.) The average diameter of the microspheres was 16 μm. When injected into the systemic circulation from the left ventricle, these microspheres were clogged in the capillary bed because the diameter of the capillary is less than 10 μm and were thus absent in the venous blood. Therefore, good contrast between arterial blood and venous blood was created for postmortem fluorescence imaging. In Fig. 20(C), the venules in the fluorescent image were pseudo-colored blue and overlaid onto a white-light image, in which all vessels were pseudo-colored red. Some vessel features, numbered 1-5, match correctly with those in Fig. 18(B), which proves that the vessels with high and low SO_2 measurements are arterioles and venules, respectively.

A further confirmation of this venule and arteriole separation is given by histology. Fig. 20(D) gives a HE-stained section showing the vessel structure at the location marked with a dashed line in Fig. 20(C), where the arteriole and venule can be distinguished by their wall thicknesses.

4. Dynamic SO_2 imaging

A Sprague Dawley rats with a body weight of ~150 g, we used in dynamic SO_2 imaging. Three physiological states (hyperoxia, normoxia and hypoxia) were introduced by controlling the oxygen concentration in the inhaled gases (pure oxygen, normal air, and carbogen consisting of 5% O_2, 5% CO_2 and 90% N_2). For each of the three states, PAM images were acquired to calculate the SO_2 at the same four wavelengths as in the static SO_2 study. After the experiment, the rats recovered normally without noticeable health problems.

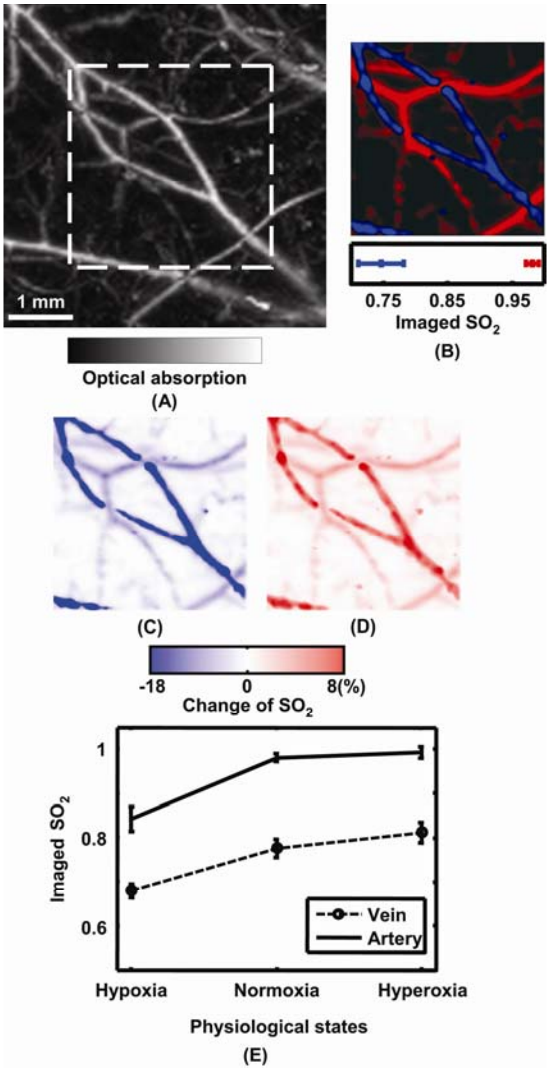

Fig. 21. Vessel-by-vessel imaging of dynamic SO_2 *in vivo*. (A) A structural MIP image. (B) A static SO_2 image within the marked region in panel A under normoxia. (C) Image of the SO_2 changes from normoxia to hypoxia. (D) Image of SO_2 changes from normoxia to hyperoxia. (E) Typical imaged values of SO_2 in venous and arterial bloods under all three physiological states.

Static SO_2 values for each physiological state were calculated on a single vessel basis. The same compensation (as stated in static SO_2 imaging) was applied to all of the three physiological states in order to assure that the imaged variations were caused only by real changes in the SO_2. Then dynamic variations in SO_2 between the physiological states were imaged on a vessel-by-vessel basis.

Similar that in static SO_2 imaging, Fig. 21(A) shows the structural MIP image of subcutaneous vessels under the hyperoxia, which was acquired at the 584-nm wavelength. Fig. 21(B) gives the result of venlue and arteriole separation under the normoxia, whose SO_2 values are given in the colorbar. Fig. 21(C) and 21(D), respectively, show the differential MIP images of the SO_2 changes from normoxia to hypoxia (hypoxia value – normoxia value) and from normoxia to hyperoxia (hyperoxia value – normoxia value) in single vessels. In this special case, the typical imaged values of SO_2 in venous and arterial bloods under all three physiological states are given in Fig. 3(E) for comparison. The imaged changes of SO_2 in the arterioles matched the Oximeter readings and other published data.[88-90]

Although the same compensation was applied to all the three physiological states, the systematic change of SO_2 itself does affect optical attenuation in skin. Thus, such compensation should be adjusted for different physiological states accordingly to achieve a more precise quantitative measurement. Further studies will be conducted to investigate changes in optical attenuation in dermis at different systemic blood oxygenations.

5. Volumetric SO_2 imaging

Combining the functional imaging capability of SO_2 with the volumetric imaging capability, the SO_2 is imaged in single blood vessels volumetrically.

The static results under hyperoxia in Fig. 21 were used in this study. After the PA measurement at four optical wavelengths (578, 584, 590, and 596 nm), the [HbO_2] and [HbR] were calculated in three dimensions. Then the point-by-point SO_2 was calculated only within the volume of blood vessels determined based on a segmentation of the structural image acquired at the 584-nm optical wavelength.

The arteriole-venule separation was based on the [HbR] image and the 584-nm structural image instead of the final SO_2 image in order to avoid division errors and achieve a smoother separation result. First, the venules were segmented in the [HbR] image. Ideally, such segmentation could be achieved based on a simple thresholding because the [HbR] in the venules was much higher than that in the arterioles. However, noise and errors induced by the inverse calculation of the [HbR], such as bright spots in the background, negative intensities, and discontinuities in the vessels, strongly affected the results obtained using thresholding. To solve this problem, a multiscale vesselness filtering[91] was applied to the [HbR] volume as a pre-processing. Vesselness filtering is an operation that selectively enhances only the tubular structures in volumetric data by analyzing the second-order information, *i.e.* analyzing the eigenvalues of the Hessian matrix, of the volume. Using a multisacle vesselness filter ensures that vessels of various sizes are all enhanced equally. After multisacle vesselness filtering, isolated spots in the background were removed, and discontinued vessels were connected in the [HbR] image. Then, negative intensities were set to zero, and the filtered volumetric data was linearly normalized to [0, 1]. Consequently, segmentation of the venules was achieved by setting the intensity threshold at 0.1. After segmentation, the intensities of the voxels within the venules were set to 0.2, and the intensities of the background voxels were set to 1 to create a venule mask.

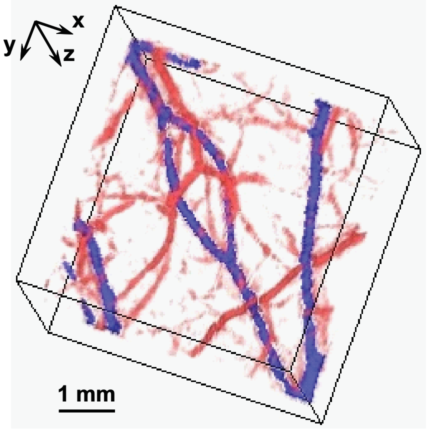

Fig. 22. Functional volumetric imaging of SO_2 in single blood vessels in rats *in vivo*. Venules and arterioles are colored blue and red, respectively.

Next, the structural image acquired at the 584-nm optical wavelength, where the PA intensities in the venules and arterioles are comparable, was linearly normalized to [32768, 65536] and multiplied by the venule mask to generate a histogram-separated image where the venules had a much lower intensity than either the arterioles or the background.

Finally, the venules and arterioles were colored blue and red, respectively, based on the separated histogram. The opacity of the vessels was set to 1, and the opacity of the background was set to less than 0.01. In Fig.22, the arterioles and venules are shown to be at different depths.

6. Discussion

These two sets of *in vivo* experiments demonstrated the unique feature of PAM, the ability to image SO_2 with high spatial resolution, high sensitivity, and high specificity in single vessels. It makes PAM a potentially powerful tool for physiological studies. In some tumor angiogenesis imaging, PAM can be used to observe, not only the morphology of newly grown vessels, but also the oxygen consumption of a tumor at different stages of growth. It can also be used to evaluate the effect of certain tumor treatments since tumor hypoxia is the primary resistance to therapeutic methods. In wound healing imaging, PAM can be used to monitor tissue regeneration, which is accompanied by higher SO_2 levels as well as the formation of new blood vessels. Another important application of PAM is the imaging of brain functions in response to sensory stimulations. It has been observed that sensory stimulations result in a quick drop followed by a gradual increase of oxygenation that usually lasts several seconds in the corresponding brain cortex. Since PAM can finish one A-line acquisition within a few microseconds, it can provide very high temporal resolution in SO_2 imaging for time course studies. Moreover, because the thickness of the brain cortex is more than 1.5

mm,[92] PAM has a significant advantage over the current widely accepted optical method due to its large imaging depth.

However, functional imaging using PAM is not limited to determining levels of SO_2. By tuning the optical wavelength towards other endogenous pigments or extrinsic contrast agents, PAM can be adapted to other applications such as melanoma imaging and genetic imaging.

CHAPTER V

HUMAN IMAGING

The ultimate aim for a developing imaging modality is to be adapted into clinics for human imaging. Since PAM requires an excitation energy density of only 6 mJ/cm^2 on the skin surface and around the optical focus, which is well within the ANSI safety standard (20 mJ/cm^2) in our imaging spectral range, it is safe for human imaging.

In the first human PAM imaging test, the total hemoglobin concentration in subcutaneous vasculature, which reflects the volumetric morphology, of a human palm was acquired at the 584-nm optical wavelength. At this wavelength, total hemoglobin concentration was imaged and comparable image quality with that from the animal studies was achieved. Fig. 23(A) gives a photograph of the imaged area. Fig. 23 (B) shows the MIP image of the PA amplitude below the stratum-corneum layer projected along the z axis. Fig. 23 (C) is the B-scan image in the z-x plane at the location indicated by the dashed line in Fig. 23 (B). The skin surface and the stratum corneum as well as blood vessels are visualized. Numbers 1-6 indicate the corresponding vessels in the MIP and B-scan images. A series of MIP images from different layers parallel with the skin surface are shown in Fig. 23 (C). The first layer starts from 0.17 mm beneath the skin surface, and the layer spacing is 0.13 mm. The largest vessel in the image is approximately 350 µm in diameter, whereas the smallest is smaller than 50 µm. The average ratio of the vessel to the background in PA signal amplitude is 35±2, and the contrast-to-noise ratio is 51 dB on average. A complete 3D visualization is given in Fig.

24. Besides the imaging of subcutaneous blood vessels of human palm, PAM was also applied to image the layered skin structure of a human finger tip (Fig. 25). The imagined superficial structures compared favorably to other published results using OCT.[93,94] However, PAM imaged much deeper than those of OCT and revealed blood vessels.

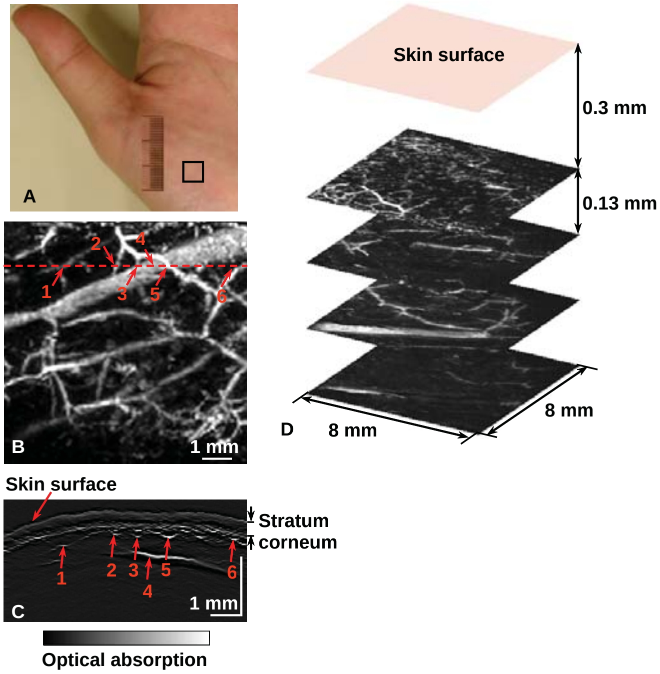

Fig. 23. *In vivo* PAM imaging of a human palm. (A) Photograph of the imaged area. (B) The total MIP image below the stratum-corneum layer. (C) The B-scan image at the location indicated by the dashed line in panel B. (D) A series of layered MIP images.

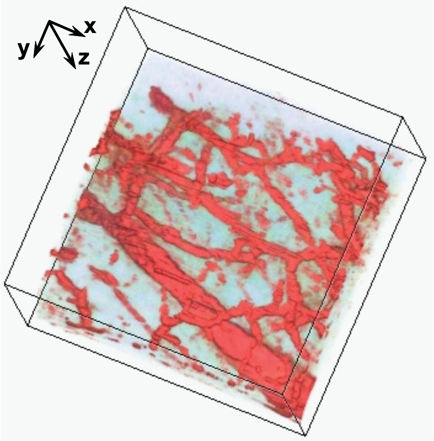

Fig. 24. A 3D rendering of the human palm imaged by PAM.

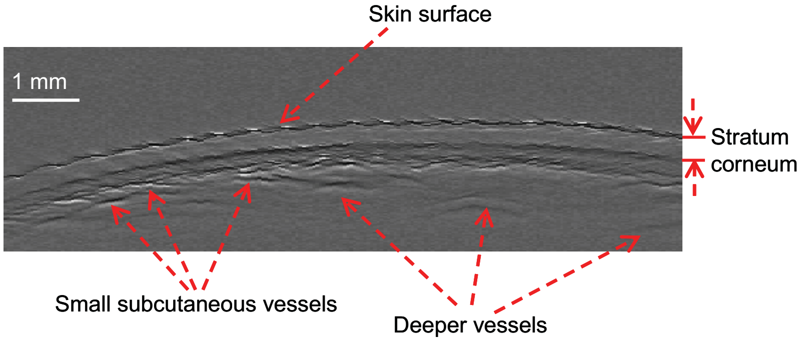

Fig. 25. PAM imaging of a human finger tip *in vivo*.

CHAPTER VI

CONCLUSION AND FUTURE WORK

1. Conclusion

A comparison of PAM with modern high-resolution microscopic imaging modalities, whose depth-to-resolution ratios are all greater than 100, is given in Table 1. We believe that PAM is a promising technique for both basic research and clinical applications, by providing complementary information to those widely accepted modalities.

First of all, we have shown that PAM breaks through the current fundamental depth limit of high-resolution optical imaging modalities while keeping the depth-to-resolution ratio greater than 100. This ratio could be maintained for an imaging depth of up to several centimeters, which is limited by the penetration depth of diffused light, and for a spatial resolution of up to a few micrometers, which is limited by the excessively strong ultrasonic attenuation at ultrasonic frequencies above a few hundred MHz. Currently, the axial resolution is 15 µm, the lateral resolution is 45 µm, and the maximum imaging depth is more than 3 mm.

Second, we, using PAM, extract functional parameters based on physiologically specific optical absorption contrast. PAM is able to provide multi-purpose functional imaging solely depends on intrinsic contrast. However, PAM is also capable of employing various optical contrast agents to conduct molecular imaging or genetic imaging.

Third, we have proven that PAM's tunability of optical wavelength and scalability of spatial resolution and imaging depth provide great flexibility for different imaging purposes. Based on spectroscopic measurement, concentrations of different optical absorption pigments, such as HbR and HBO_2, have been quantified, which provides the basis of functional imaging. The axial resolution and maximum imaging depth have been shown to be scalable with the central frequencies and bandwidths of the ultrasonic detectors.

Table 1. Comparison among the modern high-resolution microscopic imaging techniques. Year: years when the technology was developed. Depth: maximum imaging depth. Contrast: image contrast mechanisms.

Modality	Year	Depth	Contrast
Confocal microscopy	1970s	~0.5 mm	Scattering, fluorescence
Two-photon microscopy	1990s	~0.5 mm	Fluorescence
Optical coherence tomography	1990s	~1 mm	Scattering, polarization
Functional PAM	2005	~3 mm, scalable	Absorption

Finally, we have demonstrated that PAM is safe for human imaging and applicable for clinical environments. In addition to the capabilities demonstrated above, PAM will undoubtedly find broader applications, for example, in tumor studies, where angiogenesis is highly correlated with cancer aggressiveness; in neuroscience, where hemoglobin oxygen saturation is related to neural activities; in the radiotherapy and chemotherapy of cancer, where hypoxia is responsible for resistance to therapy; as well as in trauma evaluation, where optical absorption is associated with both hemorrhage and edema. Potentially, PAM can also be used in endoscopic imaging when miniaturized optical and ultrasonic components are integrated into a single probe.

2. Future work

There are several technical aspects need to be improved. First of all, current PAM is slow. The reason comes from the low laser repetition rate, which is 10 MHz. If a 50-μm scanning step is used, a B-scan image that covers a 10-mm length takes about 20 seconds; and a full 3D volume image covering 10×10×3 mm^3 takes about 60 minutes. To speed up the image acquisition, we will employ a high-repetition laser. A new version of PAM with a laser repetition rate up to 1 kHz is under construction. With such a high repetition rate, the image acquisition for a B-scan can be reduced to less than one second. Furthermore, if a high frequency ultrasonic array is employed, real-time imaging will be possible.

Second, current PAM is a table-top experimental prototype, which lacks flexibilities to image various body parts, such as shoulder or back. To solve this problem, a hand-held version of PAM is being built, which will be operated similarly as a traditional ultrasound imager to achieve maximum flexibility.

REFERENCES

1. L. V. Wang, “Ultrasound-mediated biophotonic imaging: A review of acousto-optical tomography and photo-acoustic tomography,” Dis. Markers **19**, pp. 123–138 (2004).
2. D. Bicout, C. Brosseau, A. S. Martinez, and J. M. Schmitt, “Depolarization of multiply scattered waves by spherical diffusers: influence of the size parameter,” Phys. Rev. E **49**, 1767–1770 (1994).
3. J. R. Mourant, M. Canpolat, C. Brocker, O. Esponda-Ramos, T. M. Johnson, A. Matanock, K. Stetter, and J. P. Freyer, “Light scattering from cells: the contribution of the nucleus and the effects of proliferative status,” J. Biomed. Opt. **5**, 131–137 (2000).
4. J. R. Mourant, I. J. Bigio, J. Boyer, R. L. Conn, T. Johnson, and T. Shimada, “Spectroscopic diagnosis of bladder cancer with elastic light scattering,” Lasers Surg. Med. **17**, 350–357 (1995).
5. C. G. A. Hoelen, F. F. M. de Mul, R. Pongers, and A. Dekker, “Three-dimensional photoacoustic imaging of blood vessels in tissue,” Opt. Lett.**23**, 648–650 (1998).
6. A. A. Oraevsky, V. A. Andreev, A. A. Karabutov, D. R. Fleming, Z. Gatalica, H. Singh, and R. O. Esenaliev, “Laser opto-acoustic imaging of the breast: detection of cancer angiogenesis,” Proc. SPIE **3597**, 352–363 (1999).

7. G. A. Millikan, “The oximeter, an instrument for measuring continuously the oxygen saturation of arterial blood in man,” Rev. Sci. Instrum. **13**, 434 –444 (1942).

8. F. F. Jöbsis, “Noninvasive, infrared monitoring of cerebral and myocardial oxygen sufficiency and circulatory parameters,” Science **198**, 1264 –1267 (1977).

9. T. Wilson, and C. Sheppard, Theory and Practice of Scanning Optical Microscopy (Academic Press, London, 1984).

10. A. E. Dixon, S. Damaskinos, M. R. Atkinson, “A scanning confocal microscope for transmission and reflection imaging,” Nature **351**, 551–553 (1991).

11. D A. Sipkins, X. Wei, J. W. Wu, J. M. Runnels, D. Côté, T. K. Means, A. D. Luster, D. T. Scadden, and C. P. Lin, “*In vivo* imaging of specialized bone marrow endothelial microdomains for tumour engraftment,” Nature **435**, 969–973 (2005).

12. W. Denk, J. H. Strickler, W. W. Webb, “Two-photon laser scanning fluorescence microscopy,” Science **248**, 73–76 (1990).

13. P. T. C. So, C. Y. Dong, B. R. Masters, K. M. Berland, “Two-photon excitation fluorescence microscopy,” Annu. Rev. Biomed. Eng. **2**, 399–429 (2000).

14. D. Huang, E. A. Swanson, C. P. Lin, J. S. Schuman, W. G. Stinson, W. Chang, M. R. Hee, T. Flotte, K. Gregory, C. A. Puliafito, and J. G. Fujimoto, “Optical coherence tomography,” Science **254**, 1178–1181 (1991).

15. F. A. Duck, Physical Properties of Tissue (Academic Press, London, 1990).

16. D. A. Boas, D. H. Brooks, E. L. Miller, C. A. DiMarzio, M. Kilmer, R. J. Gaudette, Q. Zhang, “Imaging the body with diffuse optical tomography,” IEEE Signal Processing Mag. **18**, 57–75 (2001)

17. R. A. Kruger, D. R. Reinecke, and G. A. Kruger, “Thermoacoustic computed tomography–technical considerations,” Med. Phys. **26**, 1832–1837 (1999)

18. R. O. Esenaliev, A. A. Karabutov, and A. A. Oraevsky, “Sensitivity of laser optoacoustic imaging in detection of small deeply embedded tumors,” IEEE J. Sel. Top. Quant. **5**, 981–988 (1999).

19. K. P. Köstli, D. Frauchiger, J. J. Niederhauser, G. Paltauf, H. P. Weber, and M. Frenz, “Optoacoustic imaging using a three-dimensional reconstruction algorithm,” IEEE J. Sel. Top. Quant. **7**, 918–923 (2001).

20. X. Wang, Y. Xu, M. Xu, S. Yokoo, E. S. Fry, and L.-H. Wang, “Photoacoustic tomography of biological tissues with high cross-section resolution: reconstruction and experiment,” Med. Phys. **29**, 2799–2805 (2002)

21. X. Wang, Y. Pang, G. Ku, X. Xie, G. Stoica, and L. V. Wang, “Non-invasive laserinduced photoacoustic tomography for structural and functional imaging of the brain in vivo,” Nat. Biotechnol. **21**, 803–806 (2003).

22. X. Wang, Y. Pang, G. Ku, G. Stoica, and L. V. Wang, “Three-dimensional laserinduced photoacoustic tomography of the mouse brain with the skin and skull intact,” Opt. Lett. **28**, 1739–1741 (2003).

23. X. Wang, G. Ku, M. A. Wegiel, D. J. Bornhop, G. Stoica, and L. V. Wang, “Noninvasive photoacoustic angiography of animal brains *in vivo* with nearinfrared light and an optical contrast agent,” Opt. Lett. **29**, 730–732 (2004).
24. K. Maslov, G. Stoica, and L. V. Wang, “*In vivo* dark-field reflection-mode photoacoustic microscopy,” Opt. Lett. **30**, 625–627 (2005)
25. H. F. Zhang, K. Maslov, G. Stoica, and L. V. Wang, “Functional photoacoustic microscopy,” Nat. Biotechnol., doi: 10.1038/nbt1220 (2006).
26. L. V. Wang, S. L. Jacques, and X. Zhao, “Continuous-wave ultrasonic modulation of scattered laser light to image objects in turbid media,” Opt. Lett. **20**, 629–631 (1995).
27. L. V. Wang, “Mechanisms of ultrasonic modulation of multiply scattered coherent light: an analytic model,” Phys. Rev. Lett. **87**, 043903-(1–4) (2001).
28. S. Sakadzic, and L. V. Wang, “High-resolution ultrasound-modulated optical tomography in biological tissues,” Opt. Lett. **29**, 2770–2772 (2004).

29 T. Sun, and G. J. Diebold, “Generation of ultrasonic waves from a layered photoacoustic source,” Nature **355**, 806–808 (1992).

30. A. C. Tam, “Applications of photoacoustic sensing techniques,” Rev. Mod. Phys. **58**, 381–431 (1986).
31. V. E. Gusev, and A. A, Karabutov, Laser Optoacoustics, (American Institute of Physics, New York, 1993).

32. R. O. Esenaliev, F. K. Tittel, S. L. Thomsen, B. Fornage, C. Stelling, A. A. Karabutov, and A. A. Oraevsky, "Laser optoacoustic imaging for breast cancer diagnostics: limit of detection and comparison with x-ray and ultrasound imaging," Proc. SPIE **2979**, 71–82 (1997).

33. V. G. Andreev, A. A. Karabutov, and A. A. Oraevsky, "Detection of ultrawide-band ultrasound pulses in optoacoustic tomography," IEEE T. Ultrason. Ferr. Control **50**, 1383–1390 (2003).

34. A. Beenen, G. Spanner, and R. Niessner, "Photoacoustic depth-resolved analysis of tissue models," Appl. Spectrosc. **51**, 51–57 (1997).

35. A. A. Oraevsky, R. O. Esenaliev, and A. Karabutov, "Laser optoacoustic tomography of layered tissues: signal processing," Proceeding of SPIE **2979**, 59–70 (1997).

36. A. A. Karabutov, E. V. Savateeva, and A. A. Oraevsky, "Imaging of layered structures in biological tissues with opto-acoustic front surface transducer," Proc. SPIE **3601**, 284–295 (1999).

37. G. Paltauf and H. Schmidt-Kloiber, "Optical method for two-dimensional ultrasonic detection," Appl. Phys. Lett. 75, 1048–1050 (1999).

38. R. G. M. Kolkman, E. Hondebrink, W. Steenbergen, and F. F. M. de Mul, "*In vivo* photoacoustic imaging of blood vessels using an extreme-narrow aperture sensor," IEEE J. Sel. Top. Quant. **9**, 343–346 (2003).

39. R. Fainchtein, B. J. Stoyanov, J. C. Murphy, D. A. Wilson, and D. F. Hanley, “Local determination of hemoglobin concentration and degree of oxygenation in tissue by pulsed photoacoustic spectroscopy,” Proc. SPIE **3916**, 19–33 (2000).
40. R. O. Esenaliev, I. V. Larina, K. V. Larin, D. J. Deyo, M. Motamedi, and D. S. Prough, “Optoacoustic technique for noninvasive monitoring of blood oxygenation: a feasibility study,” Appl. Optics **41**, 4722–4731 (2002).
41. R. O. Esenaliev, Y. Y. Petrov, O. Hartrumpf, D. J. Deyo, and D. S. Prough, “Continuous, noninvasive monitoring of total hemoglobin concentration by an optoacoustic technique,” Appl. Optics **43**, 3401–3407 (2004).
42. Y. Y. Petrov, D. Prough, D. J. Deyo, M. Klasing, M. Motamedi, and R. O. Esenaliev, “Optoacoustic, noninvasive, real-time, continuous monitoring of cerebral blood oxygenation: an *in vivo* study in sheep,” Anesthesiology **102**, 69–75 (2005).
43. X. Wang, X. Xie, G. Ku, L. V. Wang, and G. Stoica, “Non-invasive imaging of hemoglobin concentration and oxygenation in the rat brain using high-resolution photoacoustic tomography,” J. Biomed. Opt. **11**, 024015 (2006).
44. A. A. Oraevsky, and A. A. Karabutov, “Optoacoustic Tomography,” in Biomedical Photonics Handbook, Edited by T. Vo-Dinh, Vol. PM125, Chapter 34 (CRC Press, Boca Raton, FL, 2003).
45. A. Briggs, Acoustic Microscopy, (Clarendon Press, Oxford, 1992).

46. American National Standards Institute, American national standard for the safe use of lasers. ANSI Standard Z136.1-2000. (ANSI, Inc., New York, NY, 2000)

47. T. Baldeweck, P. Laugier, and G. Berger, “An *in vitro* study on porcine skin: attenuation profile estimation using auto-regressive modeling,” IEEE Proc. Ultrason. Symps. 1995 **2**, 1141–1144 (1995).

48. A. F. Frangi, W. J. Niessen, K. L. Vincken, and M. A. Viergever, “Multiscale vessel enhancement filtering,” Medical Image Computing and Computer-Assisted Intervention - MICCAI'98 Lecture Notes in Computer Science **1496**, 130–137 (1998).

49. VolView, Kitware Inc., www.volview.com (2005).

50. M. Chen, A. E. Kaufman, and R. Yagel, Volume Graphics, (Springer, London, 2000).

51. National Institutes of Health, Guide for the Care and Use of Laboratory Animals, NIH Pub. 86-23, (U.S. Government Printing Office, Washington DC, 1985).

52 M.-L. Li, H. F. Zhang, K. Maslov, G. Stoica, and L. V. Wang, “Improved *in-vivo* photoacoustic microscopy based on a virtual detector concept,” Opt. Lett. **31**, 474–476 (2006).

53. P. Carmeliet, R. K. Jain, “Angiogenesis in cancer and other diseases,” Nature **407**, 249–257 (2000).

54. J. G. Fujimoto, “Optical coherence tomography for ultrahigh resolution *in vivo* imaging,” Nature Biotechnol. **21**, 1361–1367 (2003).

55. J. A. Izatt, M. D. Kularni, S. Yazdanfar, J. K. Barton, and A. J. Welch, "*In vivo* bidirectional color Doppler flow imaging of picoliter blood volumes using optical coherence tomography," Optics. Lett. **22**, 1439–1441 (1997).
56. D. M. McDonald, P. L. Choyke, ˝Imaging of angiogenesis: from microscope to clinic,˝ Nature Med. **9**, 713–725 (2003).
57. D. Heimbach, L. Engrav, B. Grube, and J. Marvin, "Burn depth: a review," World J. Surg. **16**, 10–15 (1992).
58. B. S. Atiyeh, S. W. Gunn, and S. N. Hayek, "State of the art in burn treatment," World J. Surg. **29**, 131–148 (2005).
59. A. Watts, M. Tyler, M. Perry, A. Roberts, and D. McGrouther, "Burn depth and its histological measurement," Burns **27**, 154–160 (2001).
60. D. Park, J. Hwang, K. Jang, D. Han, K. Ahn, and B. Baik, "Use of laser Doppler flowmetry for estimation of the depth of burns," Plast. Reconstr. Surg. **101**, 1516–1523 (1998).
61. S. Srinivas, J. de Boer, H. Park, K. Keikhanzadeh, H. Huang, J. Zhang, W. Jung, Z. Chen, and J. Nelson, "Determination of burn depth by polarization-sensitive optical coherence tomography," Optics J. Biomed. Opt. **9**, 207–212 (2004).
62. S. Jiao, W. Yu, G. Stoica, and L. V. Wang, "Phase-based polarization contrast Mueller optical coherence tomography and application in burn imaging," Appl. Opt. **42**, 5191–5197 (2003).

63. J. M. Still, E. J. Law, K. G. Klavuhn, T. C. Island, and J. Z. Holtz "Diagnosis of burn depth using laser-induced indocyanine green fluorescence: a preliminary clinical trail," Burns **27**, 364–371 (2001).

64. S. Thomsen, H. Vijverberg, R. Huang, and J. Schwartz, "Changes in optical properties of rat skin during thermal coagulation," SPIE Proc. **1882**, 230–236 (1993).

65. A. R. Moritz, "Studies of thermal injury III. The pathology and pathogenesis of cutaneous burns an experimental study," Am. J. Pathol. **23**, 915–941 (1947).

66. S. Sato, M. Yamazaki, D. Saitoh, H. Tsuda, Y. Okada, M. Obara, and H. Ashida, "Photoacoustic diagnosis of burns in rats," J. Trauma **59**, 1450–1455 (2005).

67. M. Yamazaki, S. Sato, H. Ashida, D. Saito, Y. Okada, and M. Obara, "Measurement of burn depth in rats using multiwavelength photoacoustic depth profiling," J. Biomed. Opt. **10**, 064011 1–4 (2005).

68. A. R. Moritz, and F. C. Henriques, "Studies of thermal injury II. The relative importance of time and surface temperature in the causation of cutaneous burns," Am. J. Pathol. **23**, 695–720 (1947).

69. T. Baldeweck, P. Laugier, and G. Berger, "An *in vitro* study on porcine skin: attenuation profile estimation using auto-regressive modeling," IEEE Proc. of Ultrason. Symps. 1995 2, 1141–1144 (1995).

70. B.-M. Kim, S. L. Jacques, S. Rastegar, S. Thomsen, and M. Motamedi, "Nonlinear finite-element analysis pf the role of dynamic changes in blood perfusion and

optical properties in laser coagulation of tissue," IEEE J. Sel. Top. Quant. Electron. **2**, 922–933 (1996).

71. Y. Ueda, S. Sato, H. Ashida, H. Ooigawa, H. Nawashiro, K. Shima, D. Saitoh, Y. Okada, and M. Obara, "Transcranial measurement of diffuse light reflectance from cold-injured brains in rats," J. Biomed. Opt. **10**, 064010-1–7 (2005).
72. A. Tandara, and T. Mustoe, "Oxygen in wound healing—more than a nutrient," World J. Surg. **28**, 294–300 (2004).
73. I. Vanzetta and A. Grinvald, "Increased crrtical oxidative metabolism due to sensory stimulation: implications for functional brain imaging," Science **286**, 1555–1558 (1999).
74. C. Chandrakala, and D. L. Fraker, "Tumor oxygenation status as a prognostic marker," Cancer Lett. **211**, 225–235 (2005).
75. S. S. Foo, D. F. Abbott, N. Lawrentschuk, and A. M. Scott, "Functional imaging of intratumoral hypoxia," Mol. Imaging Biol. **6**, 291–305 (2004).
76. H. Liu, D. A. Boas, Y. Zhang, A. G. Yodh, and B. Chance, "Determination of optical properties and blood oxygenation in tissue using continuous NIR light," Phys. Med. Biol. **40**, 1983–1993 (1995).
77. M. Neeman, H. Dafni, O. Bukhari, R. D. Braun, and M. W. Dewhirst, "*In vivo* BOLD contrast MRI mapping of subcutaneous vascular function and maturation: validation by intravital microscopy," Magn. Reson. Med. **45**, 887–898 (2001).

78. B. Gallez, C. Baudelet, and B. F. Jordan, "Assessment of tumor oxygenation by electron paramagnetic resonance: principles and applications," NMR Biomed. **17**, 240–262 (2004).

79. J. S. Lewis, and M. J. Welch, "PET imaging of hypoxia," Q. J. Nucl. Med. **45**, 183–188 (2001).

80. B. Chance, E. Borer, A. Evans, G. Holtom, J. Kent, M. Maris, K. Mccully, J. Northrop, and M. Shinkwin, "Optical and nuclear-magnetic-resonance studies of hypoxia in human tissue and tumors," Ann NY Acad. Sci. **551**, 1–16 (1988).

81. K. Maslov, M. Sivaramakrishnan, H. F. Zhang, G. Stoica, and L. V. Wang, "Technical considerations in quantitative blood oxygenation measurement using photoacoustic microscopy *in vivo*," SPIE Proc. **6086**, 6086R1–R11 (2006).

82. S. L. Jacques and S. A. Prahl, "Absorption Spectra for Biological Tissues," (Oregon Medical Laser Center, Portland, OR, 2004), http://omlc.ogi.edu/spectra/hemoglobin/index.html.

83. W. G. Zijlstra, A. Buursma and O. W. van Assendelft, Visible and near infrared absorption spectra of human and animal hemoglobin, determination and application, (VSP, Zeist, Netherlands, 2000).

84. P. Scheid, and M. Meyer, "Mixing technique for study of oxygen-hemoglobin equilibrium: a critical evaluation," J. Appl. Physiol. **45**, 818822 (1978).

85. M. Tsao, S. Sethna, C. Sloan, and L. Wyngarden, "Spectrophotometric determination of the oxygen saturation of whole blood," J. Biol. Chem. **217**, 479–488 (1955).

86. David Jensen, The principles of physiology, (Appleton-Century-Crofts, New York, 1976).

87. P. Scheid, and M. Meyer, "Mixing technique for study of oxygen-hemoglobin equilibrium: a critical evaluation," J. Appl. Physiol. **45**, 818–822 (1978).

88. S. Kety and C. Schmidt, "The effects of altered arterial tensions of carbon dioxide and oxygen on cerebral blood flow and cerebral oxygen consumption of normal young men," J. Clin. Invest. **27**, 484–491 (1948).

89. T. Duong, C. Iadecola, and S. Kim, "Effect of hyperoxia, hypercapnia, and hypoxia on cerebral interstitial oxygen tension and cerebral blood flow," Magn. Reson. Med. **45**, 61–70 (2001).

90. T. Yoshida, M. Udo, M. Chida, M. Ichioka, and K. Makiguchi, "Effect of hypoxia on arterial and venous blood levels of oxygen, carbon dioxide, hydrogen ions and lactate during incremental forearm exercise," Eur. J. Appl. Physiol. & Occup. Physiol. **58**, 772–777 (1989).

91. A. F. Frangi, W. J. Niessen, K. L. Vincken, M. A. Viergever, "Multiscale vessel enhancement filtering," Proceedings of Medical Image Computing and Computer-Assisted Intervention, (Springer-Verlag, Berlin 1998), pp.130-137.

92. E. Sowell, P. Thompson, C. Leonard, S. Welcome, E. Kan, and A. Toga, “Longitudinal mapping of cortical thickness and brain growth in normal children,” J. Neurosci. **24**, 8223–8231 (2004).

93. M. Pircher, E. Goetzinger, R. Leitgeb, and C. Hitzenberger, “Three dimensional polarization sensitive OCT of human skin *in vivo*,” Opt. Express **12**, 3236-3244 (2004).

94. S. Yun, G. Tearney, B. Bouma, B. Park, and J. de Boer, "High-speed spectral-domain optical coherence tomography at 1.3 μm wavelength," Opt. Express **11**, 3598-3604.

APPENDIX

DATA ACQUISITION AND MOTOR CONTROLLING

The motor controlling program (Fig. 25) was coded in Turbo Pascal 7.0 under MS DOS 7.0. In order to achoeve real-time response for the commands, DOS INT21 and DOS INT17 interruptions were frequently called in the program to access the serial and parallel ports directly. The only mechanism to synchronize the motor movement with the laser pulses was the “trigger out” from either an oscilloscope or a Gage data-acquisition board. The timing between different B-scans and optical wavelength was controlled by the data acquisition program (Fig. 26) written in Matlab 7.1, which also stored the data via GPIB (for oscilloscope) or PCI (Gage card).

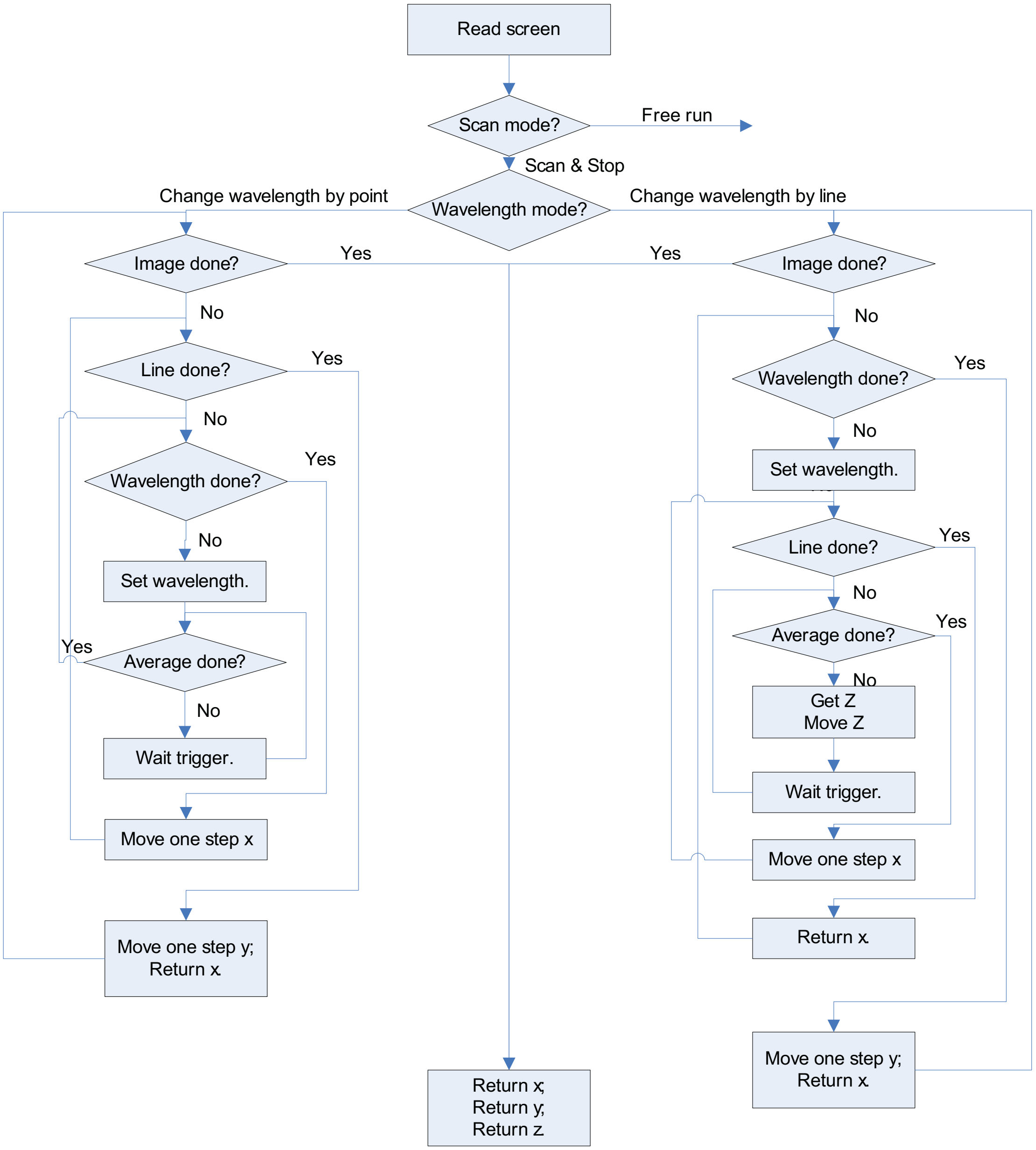

Fig. 26. Diagram of motor controlling for multi-wavelength auto-fit scan.

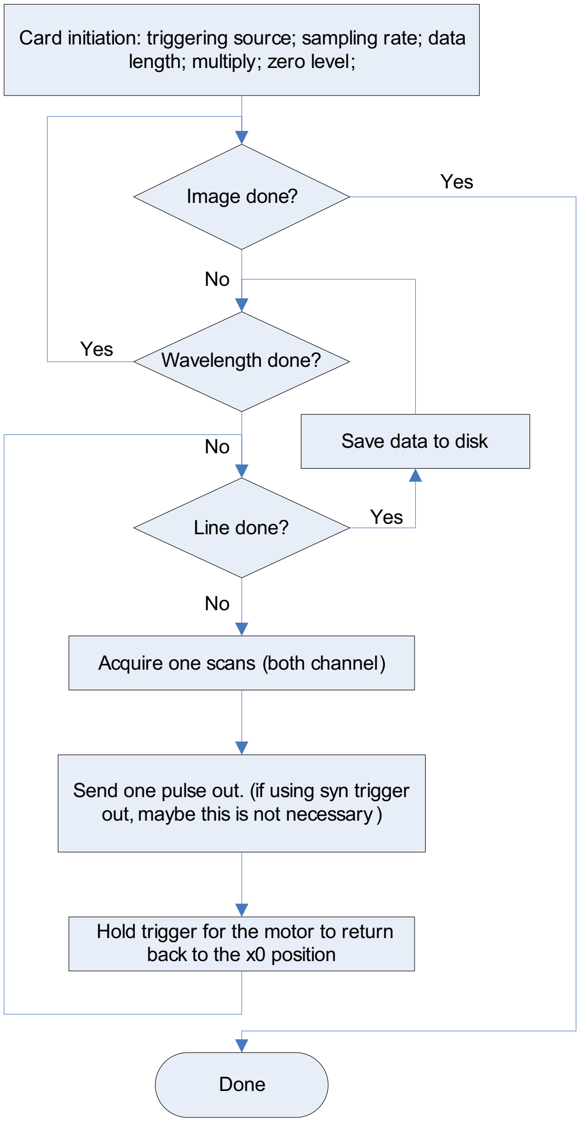

Fig. 27. Diagram of data acquisition.

VITA

CONTACT

Name: Hao Zhang
Address: 7 Linjiang Road 6-210, Wuhan, Hubei 430060, P. R. China
E-mail: yyhaofreeman@gmail.com

EDUCATION

Ph.D., Biomedical Engineering 08/2006
Texas A&M University, College Station, Texas, USA

M.Eng., Biomedical Engineering 07/2000
Shanghai JiaoTong University, Shanghai, P. R. China

B.Eng., Computer Science 07/1997
Shanghai JiaoTong University, Shanghai, P. R. China

B.Eng., Electrical Engineering 07/1997
Shanghai JiaoTong University, Shanghai, P. R. China